Evaporation-driven turbulent convection in water pools

William A. Hay[†], and Miltiadis V. Papalexandris

Université catholique de Louvain, Institute of Mechanics, Materials and Civil Engineering,
Louvain-la-Neuve, Belgium

(Received xx; revised xx; accepted xx)

In this paper we study turbulent thermal convection driven by free-surface evaporation at the top and a uniformly heated wall at the bottom. More specifically, we report on direct numerical simulations of the problem in hand over 1.25 decades of Rayleigh numbers. A shear-free boundary on top of a cubic domain acts as an approximation of a free surface. At the same location we consider different evaporation rates which form the basis of a temperature gradient assigned as a non-zero Neumann boundary condition. The corresponding lower wall temperature is fixed and we assess the thermal mixing water-side. The set-up is considered a simplified model of the turbulent natural convection in the upper volumes of spent-fuel pools of nuclear power plants. Surface temperatures are investigated over a range of 40 K, resulting in a sixteenfold increase in evaporation rates. Our work allows for the first time, analysis of the mean flow statistics of this particular thermal convection configuration. Results show that a shear-free surface increases heat transfer within the domain, however the exponent in the provided power-law relation, $Nu = 0.178Ra^{0.301}$, is similar to that of classical turbulent Rayleigh-Bénard Convection. Further, the free-slip accelerates the fluid after impingement on the upper boundary. This has a significant effect on the structure of the contained large-scale circulation. Analysis of the flow statistics then show how the shear-free surface introduces inhomogeneities in thermal boundary layer heights. Overall, the investigated turbulent convection configuration shows unique traits, borrowing from both turbulent Rayleigh-Bénard convection and evaporative cooling.

Key words: thermal convection, direct numerical simulations, turbulence, evaporative cooling, non-Oberbeck-Boussinesq conditions

1. Introduction

In this paper we report on Direct Numerical Simulations (DNS) of evaporation-driven turbulent thermal convection in a pool. With liquid water as the working medium, we approximate an evaporating free surface by imposing a heat flux at a shear-free upper boundary. Over a series of simulations we then investigate the effect of increasing evaporation rates on the flow field below. Evaporation-driven natural convection is studied extensively in oceanography but is also encountered in industrial applications such as in the spent-fuel pools of nuclear power plants.

High-temperature free-surface evaporation is of particular interest. Taking Fukushima 2011 as an example, a loss-of-cooling accident in the spent-fuel pools resulted in fuel

---

[†] Email address for correspondence: william.hay@uclouvain.be

uncovery due in part to inventory loss at sub-saturation pool temperatures. In this situation, heat is added to the upper volume of the pool from the fuel assemblies below and is predominantly evacuated via evaporation at the free surface. In the nuclear industry it is imperative to have an understanding of, and the capabilities to predict, the effect of free-surface evaporation on thermal mixing in the pool. An improved understanding will in turn lead to better predictions of the physics in the early-stages of the accident and forms the basis of the motivation for this work.

Turbulent convection and free-surface evaporation are the inter-dependent physical phenomena of interest. In order to fix ideas, consider an initially quiescent velocity field water-side. Evaporation at the free surface would induce convective motion below. This configuration is known as evaporative cooling; see figure 1a. Conversely, if heat is added from below and simultaneously evacuated above then a flow is induced similar to turbulent Rayleigh-Bénard Convection (RBC); see figure 1b. The problem in hand, shown schematically in figure 1c, can be understood as a combination of these two well-known thermal convection configurations.

Turbulent RBC is most commonly studied as a fluid uniformly heated from below and cooled from above with solid upper and lower boundaries; for reviews see Siggia (1994); Ahlers *et al.* (2009) and Lohse & Xia (2010). The flow and thermal dynamics are determined by the geometry of the system, the temperature difference across it and the resulting variation in fluid properties. The two dimensionless parameters that then govern the flow are the Prandtl, $Pr = \nu/\kappa$, and Rayleigh, $Ra = |\boldsymbol{g}|\beta \Delta T\, H^3/(\nu\kappa)$, numbers. In these expressions, $|\boldsymbol{g}|$ is the magnitude of gravitational acceleration, β the thermal expansion coefficient, H the height of the domain, ν the kinematic viscosity, ΔT the temperature difference between lower and upper boundaries and κ is the thermal diffusivity.

The system response to a given Ra and Pr is measured in terms of the dimensionless numbers for heat flux and turbulence; respectively the Nusselt (Nu) and Reynolds (Re) numbers, where the velocity for the latter is representative of the large-scale circulation (LSC) (Ahlers *et al.* 2009). This circulation, or mean wind, sweeps across the upper and lower boundaries stabilizing the thermal boundary layers, and simultaneously creating a hydrodynamic boundary layer with its shear (Sun *et al.* 2008). The shape of the container is the final control parameter which plays a particularly important role in determining the structure of the LSC. Experimental work has largely concentrated on cylindrical geometries (Chavanne *et al.* (1997); Niemala *et al.* (2000); Verzicco & Camussi (2003)), however a significant body of work also exists for the cubic domain.

Turbulent RBC in a cubic domain has been studied experimentally by Daya & Ecke (2001). Therein, measurements of velocity and temperature root-mean-square (rms) quantities in the bulk of the flow showed differences to that seen in corresponding cylindrical domains at the same Ra and Pr. This conclusion was later confirmed numerically by Foroozani *et al.* (2014) where the LSC structure in a cubic domain is also discussed further. Kaczorowski & Xia (2013) carried out highly resolved DNS of turbulent RBC in a cube for water and air over five decades of Ra, investigating velocity and temperature structure function scaling and heat transfer in the bulk. Later, Foroozani *et al.* (2017) carried out large-eddy simulations over long-time periods investigating the dynamics of LSC reorientations. They found that all flow reorientations were due to lateral rotations during which the large-scale flow entered a transient state, non-aligned with the diagonal. In this study we do not extend our DNS to such long time periods and choose time-averaging intervals that are representative of a stable LSC.

Evaporative cooling can be studied by visualizing the flow field below an evaporating interface (Spangenberg & Rowland 1961). Early observations noted that cool water

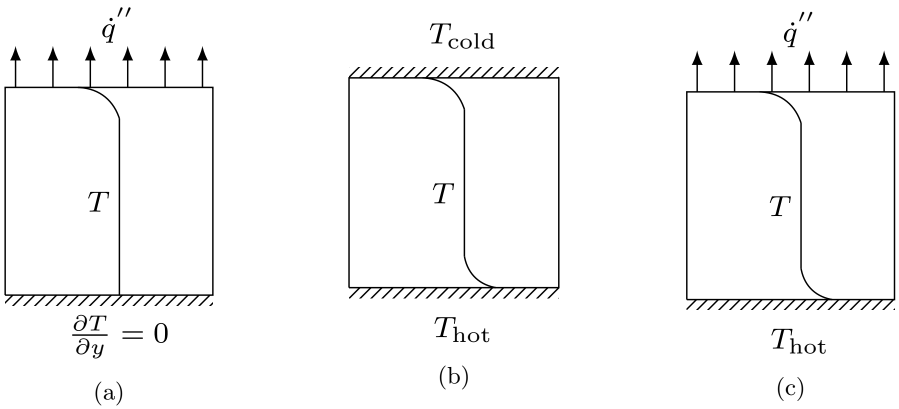

FIGURE 1. A comparison of thermal convection configurations and their temperature profiles: (a) evaporative cooling, (b) turbulent RBC, and (c) the current configuration.

accumulates along lines on the surface before plunging downwards in vertical sheets, taking surrounding fluid with it and creating an uneven surface layer. The role of an upper thermal boundary layer as a source for thermal plumes has qualitative similarities to turbulent RBC where plumes break away from a cooled upper wall, falling rapidly into the interior (Howard 1966). However, in evaporative cooling the plunging sheets are broken-up and dissipated by diffusion before interacting with an adiabatic bottom wall. There is a clear deviation from turbulent RBC here where the container bottom wall is heated and from which thermal plumes are also released from a second thermal boundary layer; see figure 1.

Further, Flack *et al.* (2001) measured velocities and subsequent turbulence quantities beneath an evaporating water surface. In that study, measurements were made for a shear-free, clean surface, i.e. without surfactants, where it was found that the turbulent kinetic energy peaked at the free surface. Volino & Smith (1999) aimed to link the surface temperature field to sub-surface velocity measurements but encountered difficulties due to sub-surface vortices interacting with the surface temperature measurements. Bukhari & Siddiqui (2006) also observed the turbulent structure beneath an air/water interface and noted that these vortices increase in number and magnitude as a result of an increasing heat flux. To the authors knowledge, no large-scale circulation has been observed in the evaporative cooling configuration. The LSC structure in the present configuration is however of interest, given the similarities with turbulent RBC.

In an earlier study, Katsaros *et al.* (1976) studied experimentally the thermal boundary layer behaviour below an evaporating water surface and also found a scaling relationship, $Nu = 0.156Ra^{0.33}$, for the evaporative cooling configuration, i.e. with a heat flux across one free boundary. Whereas, Straus (1973) derived $Ra{-}Nu$ scaling relations for turbulent RBC between two rigid plates and between two free boundaries. The exponent in both power-law scalings was the same. Much research in the turbulent RBC community has since concentrated on measuring the Nu dependence on Ra; one example (Niemala *et al.* 2000) covering a particularly large range of Ra provides $Nu = 0.124Ra^{0.309}$. The current configuration shown in figure 1c has one rigid plate and one free boundary; it is of interest therefore to find the $Ra - Nu$ scaling for this unique set-up. A comparison of both the heat transfer effectiveness and power-law exponent can then be made with similar thermal convection configurations.

The closest configuration to the one investigated in the present study is that of Zikanov *et al.* (2002). Therein, the authors studied numerically the turbulent convection occurring in warm shallow ocean during adverse weather events. A heat flux was implemented at the free-slip upper boundary to represent evaporation and the lower boundary was a rigid wall. One main difference between Zikanov *et al.* (2002) and this study is in the geometry of the domain; where Zikanov *et al.* (2002) used periodic boundaries in the horizontal directions, we have a wall-bounded domain. Further, in Zikanov *et al.* (2002) results are presented on the initial unsteady phase of the flow from a quiescent state whereas in this paper, a steady state is pursued. This produces novel Ra scaling of both Nu and a Reynolds number in the centre of the domain; enabling comparisons with similar thermal convection configurations.

An earlier thermal convection study of ours (Hay & Papalexandris 2019) assumed a fixed temperature drop across a cuboid domain while enforcing periodicity in one horizontal direction. The impact of both the free-slip and non-Oberbeck Boussinesq conditions were then assessed. The former was shown to play an important role both on Nu and on the mean temperature profile across the domain. The values for Nu were increased when compared to turbulent RBC for the same Ra; an expected result given the earlier work of Straus (1973). Moreover, the mean temperature profile was shifted towards the colder upper boundary temperature. This was the case even when considering the competing non-Oberbeck Boussinesq effects which, for the case of water as the working fluid, tends to shift the bulk temperature towards the warmer lower wall temperature. The bulk of the domain was therefore significantly cooler than that seen in turbulent RBC.

In summary, the thermal convection set-up investigated here is novel and characterized by its similarities to the well-known configurations of turbulent RBC and evaporative cooling. The configuration shown in figure 1c *has* been investigated experimentally in the past, however the aims were to measure gas-side flow and, importantly, evaporation rates (Boelter *et al.* 1946; Bower & Saylor 2009). We utilize these latter results in our study and extend the analysis water-side in order to further understanding on the role of free-surface evaporation on thermal mixing in liquid pools.

The paper is organized as follows. First we present the governing equations, followed by a detailled discussion on the estimation of evaporation rates. Next, we outline the numerical set-up and elaborate on the resolution requirements for the DNS. Subsequently, we analyse the numerical results in two parts. In the first, we provide time-averaged flow properties such as Nu, Re and the LSC structure. We then focus on the flow statistics by plotting vertical profiles of time and horizontally averaged flow properties and analyse the effect of increasing Ra, before drawing conclusions.

2. Governing equations

We consider only the flow beneath the evaporating surface and as such the working fluid is liquid water, which is treated as Newtonian. We investigate flows without invoking the Oberbeck-Boussinesq approximation and therefore take into account variations of the density and transport properties with temperature. For this reason, the system of governing equations is the low-Mach number approximation of the compressible Navier-Stokes-Fourier equations (Majda & Sethian 1985; Lessani & Papalexandris 2006),

$$\frac{\partial \rho}{\partial t} + \boldsymbol{\nabla} \cdot (\rho \boldsymbol{u}) \;=\; 0\,, \tag{2.1}$$

$$\frac{\partial\,(\rho \boldsymbol{u})}{\partial t} + \boldsymbol{\nabla} \cdot (\rho \boldsymbol{u}\boldsymbol{u}) \;=\; \boldsymbol{\nabla} \cdot \boldsymbol{\tau} - \boldsymbol{\nabla} p \,+\, \rho \mathbf{g}\,, \tag{2.2}$$

$$\frac{\partial\left(\rho c_p T\right)}{\partial t}+\boldsymbol{\nabla}\cdot\left(\rho c_p \boldsymbol{u} T\right) \;=\; \boldsymbol{\nabla}\cdot(\lambda\boldsymbol{\nabla}T)+\frac{\mathrm{d}p_0\,(t)}{\mathrm{d}t}\,, \tag{2.3}$$

where $\boldsymbol{u}=(u,v,w)$. In (2.2), p stands for the sum of the 2nd-order term of the low-Mach-number expansion of the pressure and the bulk viscous pressure (Georgiou & Papalexandris 2018; Papalexandris 2019). Also $\boldsymbol{\tau}$, stands for the deviatoric part of the viscous stress tensor, defined as $\boldsymbol{\tau}=\mu(\boldsymbol{\nabla}\boldsymbol{u}+(\boldsymbol{\nabla}\boldsymbol{u})^{\mathrm{T}}-\frac{2}{3}(\boldsymbol{\nabla}\cdot\boldsymbol{u})\mathbf{I})$, where $\mathbf{I}$ is the identity matrix and μ the dynamic viscosity.

In (2.3), c_p is the specific heat, λ the thermal conductivity and $p_0(t)$ the 1st-order component of the asymptotic expansion of pressure at the zero-Mach limit, interpreted as the thermodynamic pressure. According to the low-Mach number expansion, it is spatially uniform and a function of time only. For open domains, p_0 is equal to the ambient pressure whereas for closed domains, p_0 varies with time and can be computed from the equation of state of the working medium. In this study the domain is open. For this reason, p_0 is constant and set to the ambient pressure of one atmosphere. We note that the mass loss leaving the system due to evaporation is not modelled and the surface level is constant throughout. For the highest evaporation case the mass loss through the free-surface would be equivalent to 3%. This is considered to have a minor effect on the free surface level over the simulation times considered.

In order to close the system of governing equations, an isobaric "equation of state" for the water density is required. More specifically, a $\rho - T$ relation is introduced. This relation is a fourth-order polynomial fit (2.4) of the tabulated data in Lemmon *et al.* (2010) for water density at one atmosphere and over the temperature range of interest. The other fluid thermodynamic properties, λ and μ are also calculated from a quartic polynomial fit of the form (2.4) with data originating from the same reference. For a generic quantity ϕ, this fit reads

$$\phi \;=\; c_4T^4+c_3T^3+c_2T^2+c_1T+c_0\,. \tag{2.4}$$

An example set of coefficients for the fits of ρ/p_0, λ and μ are provided in table A1.

For the case with the largest $\varDelta T$, the dynamic viscosity and the thermal conductivity vary respectively by 24% and 2% over the temperature range of interest. In other words, even though the density variations are small, the induced variations in the transport properties of water are non-negligible. On the other hand, c_p varies by a maximum of only 0.4% over the maximum temperature range investigated. It is thus taken as a constant, case-dependent, value in all simulations; see table A1. We note that with the aforementioned variations in fluid properties, Pr varies by 26% across the domain for the highest evaporation case.

For the numerical solution of (2.1) - (2.3) we employ a second-order accurate time-integration scheme for convective and diffusive terms, taking into account the current and the two previous time steps. Regarding the spatial discretization, the governing equations are discretized using second-order central difference schemes on a collocated grid system. A flux interpolation technique is used in the spirit of Rhie & Chow (1983), to avoid pressure odd-even decoupling (Weller *et al.* 1998; Lessani & Papalexandris 2006, 2008).

For the pressure-velocity coupling a PISO-type projection method is used, similar to the methods proposed by Issa (1985) and Oliviera & Issa (2001) for incompressible flows. The divergence of the momentum equation is taken and the continuity equation is used as a constraint to formulate the variable-coefficient Poisson equation to be solved for p. In this low-Mach-number PISO algorithm, the temporal derivative of the density, $\frac{\partial\rho}{\partial t}$, emerges on the left-hand side of the Poisson equation which would be zero for the incompressible case.

3. Estimation of evaporation rates

For specified thermal boundary conditions at the walls of the pool and for given ambient conditions, the evaporation rate depends on the gas-side transport phenomena. In the present work however, the focus is not on such phenomena but on the thermal mixing water-side. For this reason, we only solve for the flow field below the free surface, referred to interchangeably herein as the interface. This in turn requires the mean temperature at the interface to be specified, from which the evaporation rates and temperature gradients at the interface can then be estimated. Also for a given mean interface temperature, the bottom-wall temperature is not known in advance and must be estimated *a priori* on a case-by-case basis. As first approximations we take estimations from high-surface temperature evaporation experiments, where data is provided for temperature drops across water domains during evaporation. These are subsequently refined in preliminary simulations until the correct temperature drop is found.

In this section we obtain realistic approximations of the heat losses at the upper boundary, as well as the corresponding lower wall temperatures. This will enable the assignment of thermal boundary conditions in the following section. To estimate these quantities we start with an energy balance across the interface which provides the following relation,

$$\dot{q}''_{\mathrm{add}} = \dot{q}''_{\mathrm{conv}} + \dot{q}''_{\mathrm{evap}} . \tag{3.1}$$

Here, the right-hand side terms, $\dot{q}''_{\mathrm{conv}}$ and $\dot{q}''_{\mathrm{evap}}$, represent respectively the convective and latent heat losses per unit surface area to the ambient gas-side environment. The left-hand side term, $\dot{q}''_{\mathrm{add}}$, represents the heat added to the interface from the water-side. By expanding this latter quantity and $\dot{q}''_{\mathrm{evap}}$, we arrive at the following,

$$\overline{\frac{\partial T}{\partial y}}\bigg|_{\mathrm{w}} = \frac{1}{\lambda_{\mathrm{w}}}\left(\dot{q}''_{\mathrm{conv}} + \dot{m}'' h_{\mathrm{lv}}\right) , \tag{3.2}$$

where $\dot{m}''$ is the evaporative mass flux, h_{lv} is the interface-temperature-dependent latent heat of evaporation and $\lambda_{\mathrm{w}}\overline{\partial T/\partial y}|_{\mathrm{w}}$ is the mean heat flux at the water-side of the interface, with λ_{w} as the thermal conductivity of water at the mean interface temperature, T_{int}. The task is then to find approximations for the right-hand side terms in (3.2) which will form the basis of our non-zero Neumann boundary condition.

As a first step in calculating $\dot{q}''_{\mathrm{evap}}$ we fix the gas-side conditions at a distance far from the interface. Estimates are taken from the experimental work of Martin & Migot (2019) investigating high temperature evaporation, with values provided in table A2. In this table, T_∞ is the temperature far from the interface and p_0 is the thermodynamic pressure. The water vapour partial pressure, $p_{\mathrm{v},\infty}$, is calculated from a Wagner equation (Poling *et al.* 2001), before taking into account the relative humidity, RH, also provided in table A2. The water vapour mass fraction far from the interface, $Y_{\mathrm{v},\infty}$, can then be found from the following relation,

$$Y_{\mathrm{v}} = \frac{p_{\mathrm{v}} M_{\mathrm{w}}}{p_{\mathrm{v}} M_{\mathrm{w}} + (p_0 - p_{\mathrm{v}}) M_{\mathrm{a}}} , \tag{3.3}$$

where M_{w} and M_{a} are respectively the molar masses of water and air. Assuming a binary mixture of water vapour and air, the mass fraction of air at the same location is found from $1 - Y_{\mathrm{v},\infty}$. The gaseous mixture density far from the interface, ρ_∞, is calculated from the mass fractions and the ideal-gas equation of state and is given in table A2. Equivalently, we set the conditions *at* the interface representative of different evaporation fluxes. First, T_{int} is selected and a corresponding saturation pressure, $p_{v,\mathrm{int}}$, is found. The

Case	Pr_f	Sc_f	Le_f	Ra_c	Sh	Ra_t	Nu_t
1	0.71	0.61	0.86	1.5×10^5	9.0	1.2×10^5	10.1
2	0.72	0.61	0.85	2.0×10^5	9.8	1.6×10^5	10.8
3	0.74	0.60	0.81	4.0×10^5	12.2	3.0×10^5	12.6
4	0.77	0.59	0.78	5.3×10^5	13.3	3.7×10^5	13.3
5	0.78	0.59	0.75	6.0×10^5	13.8	4.0×10^5	13.7

TABLE 1. Gas-side dimensionless parameters. In this table $Pr_\mathrm{f} = \nu_\mathrm{f}/\alpha_\mathrm{f}$, $Sc_\mathrm{f} = \nu_\mathrm{f}/D_\mathrm{f}$, and $Le = Sc_\mathrm{f}/Pr_\mathrm{f}$. The non-dimensional groups Ra_c, Sh, Ra_t and Nu_t are defined in the text.

vapour mass fraction, $Y_{\mathrm{v,int}}$, and mixture density, ρ_{int}, are then calculated as above with values provided in table A3.

We assume that, on the gas side, the transition from the interface conditions to those far away takes place within a layer of finite thickness, referred to herein as a *film*. Finding the mean of the interface values and those at a distance far away allows for an estimation of the film properties. We require the quantities of ρ_f, $c_{p\mathrm{f}}$, μ_f and λ_f, representing respectively the *film* density, specific heat, dynamic viscosity and thermal conductivity. Of these, both ρ_f and $c_{p\mathrm{f}}$ are mass-averaged using the film mass fraction, $Y_{\mathrm{v,f}}$, whereas the quantities of μ_f and λ_f are found from the kinetic theory of gases; see Wilke (1950) and Mason & Saxena (1958) respectively. The film diffusion coefficients for momentum, ν_f, and energy, κ_f, respectively the kinematic viscosity and the thermal diffusivity are then found from a combination of the aforementioned properties. Finally, the film mass diffusivity for the binary mixture of air and vapour, D_f, is found from the following relation (Marrero & Mason 1972),

$$D_\mathrm{f} \;=\; 1.87 \times 10^{-10}\, \frac{T_\mathrm{f}^{2.072}}{p_0} \quad \left(\frac{\mathrm{m}^2}{\mathrm{s}}\right), \tag{3.4}$$

where the thermodynamic pressure, p_0, is equal to 1 atm. The film diffusion coefficients are used to find the film Prandtl (Pr_f), Schmidt (Sc_f) and Lewis (Le_f) numbers, all of which are provided in table 1. For all cases examined herein, it was assumed that $Le = 1$, implying that the concentration and thermal boundary layer heights above the interface are equal. This allows us to find a gas-side concentration Rayleigh number using properties based on the local water vapour mass fraction and temperature.

Pertinent experimental studies of free-surface evaporation include Boelter *et al.* (1946) and Bower & Saylor (2009). Both measured evaporation rates into a quiescent air environment; however Bower & Saylor (2009) used an improved set-up, allowing for more realistic air-side natural convection conditions. Both papers provide Sherwood number (Sh) correlations based on a relationship with the Schmidt number (Sc) and the concentration Rayleigh number, Ra_c, defined as follows,

$$Ra_\mathrm{c} \;=\; \frac{|\boldsymbol{g}|\,(\rho_\infty - \rho_{\mathrm{int}})\,W^3}{D_\mathrm{f}\mu_\mathrm{f}}\,. \tag{3.5}$$

Bower & Saylor (2009) then proposed the following correlation, used here to find an estimation of the concentration boundary layer height, δ_c,

$$Sh \;=\; 0.23\; Sc^{\frac{1}{3}}\, {Ra_\mathrm{c}}^{0.321} \approx \frac{W}{\delta_\mathrm{c}}\,. \tag{3.6}$$

The fact that Sh is inversely proportional to the height of the concentration boundary layer is again an analogy with heat transfer that holds in cases with $Le = 1$. The mass

Case	$\dot{m}''$ $(\frac{\mathrm{kg}}{\mathrm{m}^2\mathrm{s}})$	$\dot{q}''_{\mathrm{evap}}$ $(\frac{\mathrm{W}}{\mathrm{m}^2})$	$\dot{q}''_{\mathrm{conv}}$ $(\frac{\mathrm{W}}{\mathrm{m}^2})$	$\overline{\frac{\partial T}{\partial y}}\Big\vert_{\mathrm{w}}$ $(\frac{\mathrm{K}}{\mathrm{m}})$
1	2.4×10^{-4}	580	90	1000
2	3.6×10^{-4}	860	130	2000
3	1.5×10^{-3}	3420	310	6000
4	2.8×10^{-3}	6480	420	10000
5	3.9×10^{-3}	9040	470	14000

TABLE 2. Fluxes at the interface. In this table $\dot{m}''$ is the mass flux, $\dot{q}''_{\mathrm{evap}}$ is the evaporative heat flux, and $\dot{q}''_{\mathrm{conv}}$ is the convective heat flux. The prescribed temperature gradient, $\overline{\partial T/\partial y|_{\mathrm{w}}}$, is the dimensional form of the non-zero Neumann upper thermal boundary condition. The values are rounded to the nearest thousand to highlight their approximate nature.

flux can then be estimated with the following relation (Lienhard & Lienhard 2019),

$$\dot{m}'' = \frac{\rho_{\mathrm{f}} D_{\mathrm{f}}}{\delta_{\mathrm{c}}} \log\left(1 + B_{\mathrm{m}}\right), \tag{3.7}$$

with the mass transfer driving force, B_{m}, defined as

$$B_{\mathrm{m}} = \left(\frac{Y_{\mathrm{v},\infty} - Y_{\mathrm{v,int}}}{Y_{\mathrm{v,int}} - 1}\right). \tag{3.8}$$

Substituting (3.6) into (3.7) gives the following relation for the mass flux,

$$\dot{m}'' = Sh \frac{\rho_{\mathrm{f}} D_{\mathrm{f}}}{W} \log\left(1 + B_{\mathrm{m}}\right). \tag{3.9}$$

The latent heat flux is then found from $\dot{q}''_{\mathrm{evap}} = \dot{m}'' h_{\mathrm{lv}}$ and the final heat and mass fluxes are provided in table 2.

Next, the convective heat loss is estimated by assuming that it is proportional to the difference between the temperature of the interface, T_{int}, and the ambient gas-side temperature, T_∞, with the heat transfer coefficient, h, as the proportionality coefficient. Overall we have the following,

$$\dot{q}''_{\mathrm{conv}} = h\left(T_{\mathrm{int}} - T_\infty\right), \tag{3.10}$$

where h is estimated from the following correlation for a horizontal flat surface that is warmer than the ambient air above (Lloyd & Moran 1974),

$$\frac{h\, W}{\lambda_{\mathrm{f}}} = Nu_{\mathrm{t}} = 0.54 Ra_{\mathrm{t}}^{\frac{1}{4}}. \tag{3.11}$$

In the above relation, Ra_{t} is the gas-side thermal Rayleigh number,

$$Ra_{\mathrm{t}} = \frac{|\boldsymbol{g}|\beta_\infty \left(T_{\mathrm{int}} - T_\infty\right) W^3}{\kappa_{\mathrm{f}} \nu_{\mathrm{f}}}, \tag{3.12}$$

and W is the characteristic length-scale, the width of the domain. We provide values for Ra_{t} and Nu_{t} in table 1 and $\dot{q}''_{\mathrm{conv}}$ in table 2.

With the upper temperature gradient known, it remains to find an estimate for the corresponding case-dependent lower-wall temperatures, T_{low}. Martin & Migot (2019) carried out evaporation experiments of water at high-surface temperatures and measured the temperature drop between the water bulk and the interface, $\Delta T_{\mathrm{u}} = T_{\mathrm{bulk}} - T_{\mathrm{int}}$. They reported that the temperature drop from the interface to the bulk increases in a non-linear manner with increasing evaporation rate. They also observed that the temperature

Case	Ra	T_{int} (K)	T_{low} (K)	T_{ref} (K)
1	7.5×10^6	313.15	315.25	314.20
2	1.5×10^7	318.15	321.65	319.90
3	5×10^7	338.15	345.15	341.65
4	9×10^7	348.15	358.15	353.15
5	1.3×10^8	353.15	365.65	359.40

TABLE 3. Thermal boundary conditions: In this table T_{int} is the predicted interface value, T_{low} is the fixed lower wall temperature, and T_{ref} is the mean pool temperature. The normalized temperature is defined as $\hat{\theta} = (T - T_{\text{ref}})/\mathit{\Delta} T$, so that the upper and lower boundary values correspond to $\hat{\theta}_{\text{int}} = -0.5$ and $\hat{\theta}_{\text{low}} = 0.5$ respectively for all cases.

drop between the heated lower wall and the bulk, $\mathit{\Delta} T_{\text{l}} = T_{\text{low}} - T_{\text{bulk}}$, was approximately equal to that between the bulk and the interface. That is, $\mathit{\Delta} T_{\text{l}} \approx \mathit{\Delta} T_{\text{u}}$. Therefore, in our configuration, the total temperature difference across the pool is first approximated as follows,

$$\mathit{\Delta} T = T_{\text{low}} - T_{\text{int}} = 2\mathit{\Delta} T_{\text{u}} , \tag{3.13}$$

with $\mathit{\Delta} T_{\text{u}}$ estimated from the experiments of Martin & Migot (2019).

This first approximation is updated in preliminary simulations until the correct time and area averaged T_{int} is found. As $\mathit{\Delta} T_{\text{u}}$ was reported to increase with evaporation rates, the lower wall temperature, T_{low} is case-dependent. A physical explanation for this is seen in (3.1), where a higher evaporation flux is only possible with more heat added to the interface from below. In the current configuration, this energy addition must be via an increase in T_{low}. The lower wall temperatures are provided in table 3, alongside the predicted time and area-averaged T_{int}.

It is worth adding here an observation of Boelter *et al.* (1946), that evaporation measurements were invalidated above an upper physical limit. In their experiments boiling at the lower wall began at bulk water temperatures in excess of 361.15 K. In table 3, we see that the T_{low} of case 5 exceeds this limit; the results for this case are therefore caveated but are included to explore the parameter space more completely. At the other end of the scale, the smallest Ra investigated herein corresponds to an interface temperature of 40 K. At lower temperatures, the associated evaporation rate produces too small a $\mathit{\Delta} T$ to drive turbulent convection below.

Finally, we define the normalized temperature as follows,

$$\hat{\theta} = (T - T_{\text{ref}})/\mathit{\Delta} T , \tag{3.14}$$

with T_{ref} as the mean of the lower wall and interface temperatures. If the estimations of the evaporative heat losses and corresponding lower wall temperatures are correct, we have $\hat{\theta}_{\text{int}} = -0.5$ and $\hat{\theta}_{\text{low}} = 0.5$, at the statistically stationary solution.

4. Numerical set-up

The computational domain is a cube of unity aspect ratio. As mentioned in the introduction, deviations away from the classical turbulent RBC set-up in the current configuration are in both the hydrodynamic and thermal boundary conditions prescribed at the upper boundary. Before expanding on this, we introduce dimensionless variables denoted by a hat $(\hat{.})$ and provide reference values used for non-dimensionalization purposes in table 4. The reference length is the height of the cube, H, and is constant for all cases. With

Ra	U_{ff} $(\frac{\mathrm{m}}{\mathrm{s}})$	$\mathit{\Delta} T$ (K)	ρ_{ref} $(\frac{\mathrm{kg}}{\mathrm{m}^3})$	λ_{ref} $(\frac{\mathrm{W}}{\mathrm{mK}})$	β_{ref} $(\frac{1}{\mathrm{K}})$	ν_{ref} $(\frac{\mathrm{m}^2}{\mathrm{s}})$	κ_{ref} $(\frac{\mathrm{m}^2}{\mathrm{s}})$	Pr_{ref}
7.5×10^6	0.019	2.1	991.8	0.63	4.0×10^{-4}	6.4×10^{-7}	1.52×10^{-7}	4.2
1.5×10^7	0.026	3.5	989.5	0.64	4.3×10^{-4}	5.8×10^{-7}	1.54×10^{-7}	3.8
5×10^7	0.042	7.0	978.6	0.66	5.6×10^{-4}	4.2×10^{-7}	1.61×10^{-7}	2.6
9×10^7	0.051	10.0	971.8	0.67	6.2×10^{-4}	3.6×10^{-7}	1.63×10^{-7}	2.2
1.3×10^8	0.060	12.5	967.8	0.68	6.4×10^{-4}	3.4×10^{-7}	1.65×10^{-7}	2.1

TABLE 4. Reference values for non-dimensionalization purposes. The reference height, H, is 0.045 m for all cases.

the reference velocity as the free-fall velocity, $U_{\mathrm{ff}} = \sqrt{|\boldsymbol{g}| H \beta_{\mathrm{ref}} \mathit{\Delta} T}$, we find a reference free-fall time from $t_{\mathrm{ff}} = H/U_{\mathrm{ff}}$. Finally, the reference temperature is the mean in the pool, T_{ref}, with all reference properties then relative to T_{ref}.

The lower wall is located at $\hat{y} = 0$, the upper boundary at $\hat{y} = 1$ and, likewise, the side walls at $\hat{x} = 0$ $(\hat{z} = 0)$ and $\hat{x} = 1$ $(\hat{z} = 1)$. No-slip velocity boundary conditions are enforced at the side and lower walls. The free-slip condition is prescribed at the upper boundary, i.e. $\frac{\partial \hat{u}}{\partial \hat{y}} = \frac{\partial \hat{w}}{\partial \hat{y}} = 0$ and $\hat{v} = 0$ at $\hat{y} = 1$. This can be considered as a first order approximation of a free surface. For the thermal boundary conditions outlined in the previous section we have adiabatic side-walls with $\frac{\partial \hat{\theta}}{\partial \hat{x}}$ prescribed. At $\hat{y} = 0$ we set $\hat{\theta} = 0.5$ as a Dirichlet boundary condition, whereas at $\hat{y} = 1$ we prescribe the non-zero Neumann conditions provided in table 2. The non-dimensional form of the prescribed temperature gradients are found by dividing by the case-specific $\mathit{\Delta} T/H$, which gives $\frac{\partial \hat{\theta}}{\partial \hat{y}} = 21.4$, 25.7, 38.6, 45.0 and 50.4 for cases 1–5 respectively.

As a result of the aforementioned boundary conditions, five hydrodynamic boundary layers exist, one at each of the vertical side walls and one at the lower wall. On the other hand, there are only two thermal boundary layers, at the cooled upper boundary and heated lower wall. Finally, and with regard to the initial conditions, a linear temperature profile from T_{low} to T_{int} is employed across the vertical direction, whereas for the velocity a quiescent field is enforced to which small random perturbations are applied.

The Rayleigh number is then calculated as follows,

$$Ra = \frac{g \beta_{\mathrm{ref}} (T_{\mathrm{low}} - T_{\mathrm{int}}) H^3}{\nu_{\mathrm{ref}} \kappa_{\mathrm{ref}}}, \tag{4.1}$$

with the $\mathit{\Delta} T$ now specific to our boundaries. We provide values for Ra in table 3 and herein refer to cases 1–5 via their corresponding Ra. An instantaneous view of typical temperature isosurfaces are presented in figure 2 for the cases of $Ra = 1.5 \times 10^7$ and $Ra = 9 \times 10^7$; smaller flow structures appear as evaporation is increased.

5. Resolution requirements

The accuracy of a DNS is ensured only when the smallest length scales of the flow are everywhere resolved. The first criterion is therefore to ensure adequate resolution of the hydrodynamic and thermal boundary layers in the vertical direction. A universal criterion based on the laminar Prandtl-Blasius boundary layer theory has been developed by Shishkina *et al.* (2010). For all cases the thermal boundary layer height is predicted as $\hat{\delta}_\theta = \frac{1}{2Nu}$.

For the cases where $Pr_{\mathrm{ref}} > 3$, the *a priori* estimate of the dimensionless hydrodynamic

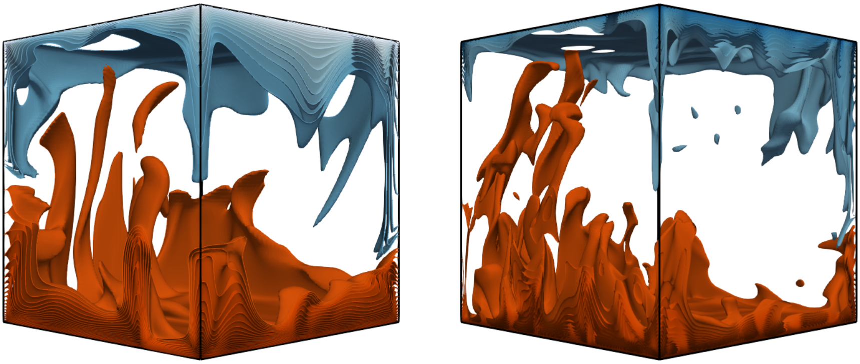
(a) (b)

FIGURE 2. Instantaneous isosurfaces of the temperature field: (a) a low evaporation case corresponding to $Ra = 1.5 \times 10^7$ and (b) a high evaporation case corresponding to $Ra = 9 \times 10^7$.

boundary layer height, $\hat{\delta}_{\boldsymbol{u}}$, is given by

$$\hat{\delta}_{\boldsymbol{u}} = \frac{1}{2} E^{-1} Nu^{-1} Pr^{\frac{1}{3}}\,, \tag{5.1}$$

where the empirical constant $E = 0.982$. Then, according to Shishkina *et al.* (2010), the minimum resolution requirements for $\hat{\delta}_{\boldsymbol{u}}$ and $\hat{\delta}_\theta$, denoted by $N_{\boldsymbol{u}}$ and N_θ respectively, are

$$N_{\boldsymbol{u}} = \sqrt{2} a E^{\frac{1}{2}} Nu^{\frac{1}{2}} Pr^{\frac{1}{3}}\,, \tag{5.2}$$

$$N_\theta = \sqrt{2} a E^{\frac{3}{2}} Nu^{\frac{1}{2}}\,, \tag{5.3}$$

where the empirical constant $a = 0.482$.

Equivalently, where $Pr_{\mathrm{ref}} < 3$, the estimate of $\hat{\delta}_{\boldsymbol{u}}$ is given by

$$\hat{\delta}_{\boldsymbol{u}} = \frac{1}{2} Nu^{-1} Pr^{0.357 - 0.022 \log Pr}\,, \tag{5.4}$$

and the minimum resolution requirements, $N_{\boldsymbol{u}}$ and N_θ, by

$$N_{\boldsymbol{u}} = \sqrt{2} a Nu^{\frac{1}{2}} Pr^{0.3215 + 0.011 \log Pr}\,, \tag{5.5}$$

$$N_\theta = \sqrt{2} a Nu^{\frac{1}{2}} Pr^{-0.0355 + 0.033 \log Pr}\,. \tag{5.6}$$

The values of $N_{\boldsymbol{u}}$ and N_θ are rounded to the next integer and are provided in table 5, where they are taken as minimum requirements for the number of points inside the boundary layers. In fact, as can be seen by the difference in values of those in parentheses and those outside, we intentionally over-resolve by a factor of two.

Further, in turbulent RBC the dissipation of turbulent kinetic energy peaks in the near-wall regions. It is therefore important to ensure that the grid is adequately refined in these regions too. Accordingly, we choose to refine equally in all directions using a hyperbolic-tangent expansion from a minimum cell size at the boundaries to a maximum in the centre of the pool. This results in $\hat{\varDelta y}_{\max} = \hat{\varDelta x}_{\max} = \hat{\varDelta z}_{\max}$ in the centre.

The second resolution criterion is to ensure that the bulk of the domain is adequately resolved. A satisfactory refinement can be predicted *a priori* by using the method of Stevens *et al.* (2010), itself based originally on Grötzbach (1983). To this end, we recall that the Kolmogorov scale η is defined as $\eta = (\nu^3/\epsilon)^{\frac{1}{4}}$, with ϵ as the kinetic-energy dissipation. Moreover, for fluids at $Pr > 1$, it is the temperature microscale and not the

Ra	$N_x \times N_y \times N_z$	$N_{\boldsymbol{u}}$	N_θ	$\hat{\Delta y}_{\min}$	$\hat{\Delta y}_{\max}$	$\frac{\Delta}{\pi\eta}$	$\frac{\Delta}{\pi\eta_\theta}$
7.5×10^6	$100 \times 100 \times 100$	10 (5)	7 (3)	0.0028	0.0171	0.22	0.65
1.5×10^7	$130 \times 130 \times 130$	12 (6)	8 (4)	0.0016	0.0144	0.25	0.68
5×10^7	$180 \times 180 \times 180$	12 (6)	9 (4)	0.0012	0.0104	0.36	0.72
9×10^7	$200 \times 200 \times 200$	12 (6)	9 (5)	0.0010	0.0094	0.44	0.76
1.3×10^8	$220 \times 220 \times 220$	12 (6)	10 (5)	0.0009	0.0087	0.46	0.75

TABLE 5. Resolution criteria. In this table N_y is minimum number of points required in the vertical direction to satisfy both bulk and boundary layer resolution requirements (we then set $N_y = N_x = N_z$), N_θ is the minimum number of points in the thermal boundary layer, $N_{\boldsymbol{u}}$ is the minimum number of points in the hydrodynamic boundary layer, $\hat{\Delta y}_{\min}$ and $\hat{\Delta y}_{\max}$ are the minimum and maximum dimensionless cell size, and the penultimate and final columns show the maximum ratio of cell size to the calculated *a posteriori* Kolmogorov and temperature microscales respectively.

Kolmogorov equivalent that is limiting. Interestingly however, the temperature microscale itself is Pr-dependent. That is, for fluids at $Pr \leqslant 1$, the relevant temperature microscale is the Corrsin scale, $\eta_{\mathrm{C}} = \eta/Pr^{\frac{3}{4}} = (\kappa^3/\epsilon)^{\frac{1}{4}}$. Whereas, for $Pr > 1$ the Batchelor scale, $\eta_{\mathrm{B}} = \eta/Pr^{\frac{1}{2}} = (\kappa^3 Pr/\epsilon)^{\frac{1}{4}}$, should be used (Tennekes & Lumley 1972). As a side-note, $\eta_{\mathrm{C}} = \eta_{\mathrm{B}}$ for the case of $Pr = 1$ (Batchelor 1959). The above analysis suggests that the relevant temperature microscale for fluids at $Pr > 1$ should always be η_{B}; however Grötzbach (1983), Stevens *et al.* (2010) and many other authors in the turbulent RBC literature use η_{C}.

Now, we let Δ be the maximum length of a given computational cell. The maximum wave-number seen by the grid, $k_{\max} = \pi/\Delta$, must then be greater than the reciprocal of the Kolmogorov and temperature microscales (Grötzbach 1983; Stevens *et al.* 2010). The combination of the above relations leads to the following constraints,

$$\Delta \leqslant \pi\eta = \pi\left(\nu^3/\epsilon\right)^{\frac{1}{4}} , \tag{5.7}$$

and either

$$\Delta \leqslant \pi\eta_{\mathrm{C}} = \pi\left(\kappa^3/\epsilon\right)^{\frac{1}{4}} , \tag{5.8}$$

or

$$\Delta \leqslant \pi\eta_{\mathrm{B}} = \pi\left(\kappa^3 Pr/\epsilon\right)^{\frac{1}{4}} . \tag{5.9}$$

For fluids at $Pr > 1$, the questionable condition (5.8) oft-used by the turbulent RBC community is nevertheless more stringent. For this reason, it is constraint (5.8) that is used from hereon based on η_{C}, with this latter quantity now referred to as the temperature microscale, η_θ.

Deardroff & Willis (1967) argued that the turbulent kinetic energy dissipation profile in turbulent RBC is flat in the bulk of the flow. This led Grötzbach (1983) to assume this dissipation to be constant and equal to the buoyant production. The hydrodynamic resolution requirement based on the smallest Kolmogorov scale is then given by,

$$\Delta \leqslant \pi\eta \approx \pi H\left(\frac{Pr^2}{Ra\,Nu}\right)^{\frac{1}{4}} . \tag{5.10}$$

Next, using the Corrsin scale relation, $\eta_\theta/\eta = Pr^{\frac{3}{4}}$, (5.10) is transformed into an thermal resolution requirement as follows,

$$\varDelta \leqslant \pi\eta_\theta \approx \pi H \left(\frac{1}{Ra\,Pr\,Nu}\right)^{\frac{1}{4}} , \tag{5.11}$$

with H as the height of the domain.

We note that a prediction of Nu is required in (5.10) and (5.11) and that, to the authors knowledge, no correlation exists in the literature for the current configuration. Previous studies showed that a first estimate for Nu can be obtained via a classical $Ra - Nu$ correlation from the literature, for example $Nu = 0.124Ra^{0.309}$ (Niemala *et al.* 2000). Increasing this value by approximately 30% then allows for the shear-free upper boundary effect to be taken into account. Preliminary simulations are then performed on a coarse grid, where coarse is defined as reducing the number of cells necessary for a resolved DNS by a factor of two in each direction, whilst still respecting the minimum boundary layer refinements in table 5.

These preliminary simulations are run until statistically steady whereupon we take statistics over 300 free-fall times and assess the time and area-averaged temperature at the upper boundary. If this value corresponds to the predicted T_{int} provided in table 3, then the Ra provided in the same table is accurate and Nu is updated in (5.10) and (5.11). The coarse grid solutions are then used for initialization purposes for the fully-resolved DNS.

The number of cells in the x, y and z directions for the fully-resolved DNS are then given respectively by N_x, N_y and N_z and are provided in table 5. In order to assess this refinement *a posteriori* we find the ratios of grid spacing to the local Kolmogorov (5.7) and temperature (5.8) microscales. The final two columns in table 5 show the maximum ratios in the domain, where all refinements are shown to be adequate, that is smaller than unity.

The time-step in our simulations is computed from a maximum Courant number of 0.25. As in Kaczorowski & Wagner (2008), the constraint on the time-step for numerical stability purposes is then stricter than that of the Kolmogorov and temperature timescales. The smallest of the flow timescales can therefore be considered well captured.

6. Numerical results and discussion

The results section is divided into two parts. First, we look at the mean flow characteristics including the structure of the LSC, measurements of the rms of vertical velocity in the bulk of the flow and the dimensionless heat transfer. We then analyse the turbulent statistics across the vertical direction and in doing so assess the impact of increasing Ra on boundary layer behaviour. The notation adopted is as follows: the mean of a generic variable ϕ is denoted by $\langle\phi\rangle$ and refers to averaging over time, additional averaging over a given horizontal $x - z$ plane is denoted by $\langle\phi\rangle_{xz}$, and over volume by $\langle\phi\rangle_{xyz}$. The fluctuating component is then denoted by ϕ' and the rms value by $\phi_{\mathrm{rms}} = \sqrt{\langle\phi'\phi'\rangle}$. The time averaging in our study was taken over 300 free-fall times which is similar to the time interval used by Kaczorowski & Xia (2013) for the range of Ra investigated. We later test the adequacy of this interval.

6.1. *Mean flow properties*

To assess the accuracy of the prescribed heat fluxes at the upper boundary, we first analyse the time and area-averaged upper boundary temperatures. Figure 3 shows the time-averaged normalized temperature at the upper boundary. We note first that

Ra	$\langle\hat{\theta}_{\mathrm{int}}\rangle_{xz}$	Nu	$\hat{\delta}_{\theta_{\mathrm{int}}}$	$\hat{\delta}_{\theta_{\mathrm{low}}}$	$\frac{1}{2Nu}$	$\hat{\delta}_{\boldsymbol{u}}$	$(v_{\mathrm{rms}})_{\mathrm{ctr}}$	Re_{ctr}	$(v_{\mathrm{rms}})_{\mathrm{xyz}}$	Re
7.5×10^6	-0.51	21.2	0.017	0.028	0.024	0.048	0.0008	56	0.0015	107
1.5×10^7	-0.49	25.9	0.014	0.021	0.019	0.040	0.0010	76	0.0021	166
5×10^7	-0.51	38.3	0.009	0.014	0.013	0.028	0.0016	168	0.0040	428
9×10^7	-0.50	44.6	0.008	0.012	0.011	0.025	0.0021	254	0.0052	647
1.3×10^8	-0.51	49.7	0.007	0.011	0.010	0.024	0.0025	326	0.0062	822

TABLE 6. Time-averaged results. Where $\langle\hat{\theta}_{\mathrm{int}}\rangle_{xz}$ is the time and area averaged normalized interface temperature, Nu is the volume and time averaged Nusselt number, $\hat{\delta}_{\theta_{\mathrm{int}}}$ and $\hat{\delta}_{\theta_{\mathrm{low}}}$ are the thermal boundary layer heights at the interface and the lower wall respectively, whereas $\hat{\delta}_{\boldsymbol{u}}$ is the hydrodynamic boundary layer height at the lower wall. $Re_{\mathrm{ctr}} = (v_{\mathrm{rms}})_{\mathrm{ctr}} H/\nu_{\mathrm{ref}}$ is the Reynolds number in the centre of the domain, where $(v_{\mathrm{rms}})_{\mathrm{ctr}} = \sqrt{\langle v'v'\rangle}_{\mathrm{ctr}}$ (m/s) is the rms of the vertical velocity in the same location. $Re = (v_{\mathrm{rms}})_{\mathrm{xyz}} H/\nu_{\mathrm{ref}}$ is the global Reynolds number where $(v_{\mathrm{rms}})_{\mathrm{xyz}} = \sqrt{\langle v'v'\rangle}_{\mathrm{xyz}}$ (m/s) is the volume-averaged rms of the vertical velocity.

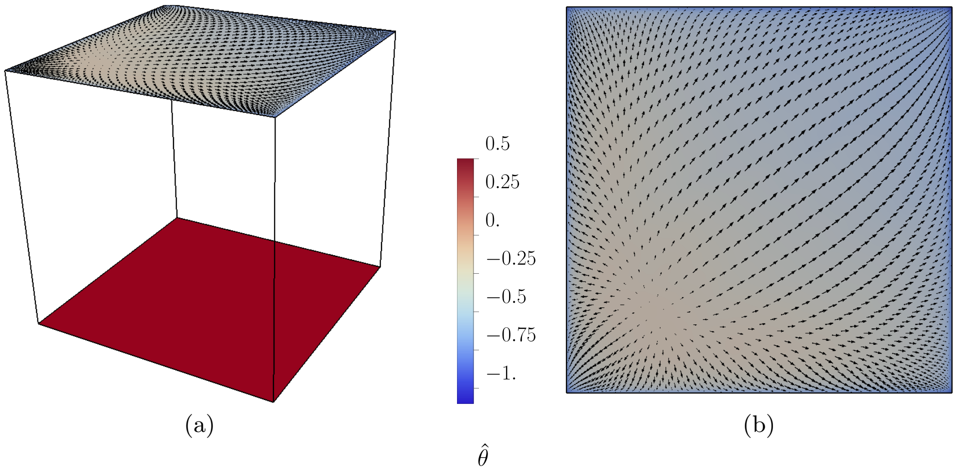

(a) (b)

FIGURE 3. Normalized temperature, $\hat{\theta}$, at the interface and lower wall for $Ra = 9 \times 10^7$: (a) side-view showing constant $\hat{\theta}_{\mathrm{low}} = 0.5$ on lower wall and spatially-variable $\hat{\theta}_{\mathrm{int}}$ on upper boundary ($-1.14 < \hat{\theta}_{\mathrm{int}} < -0.33$) and (b) Top view of upper boundary with superimposed velocity vectors showing LSC impingement and subsequent flow direction.

in turbulent RBC with fixed temperature boundary conditions the coldest physical temperature is $\hat{\theta} = -0.5$, whereas in the current configuration cold spots appear near the intersection of the upper boundary and side-walls corresponding to twice this value. However, the time and area-averaged values, $\langle\hat{\theta}_{\mathrm{int}}\rangle_{xz}$, are provided in table 6, where they are seen to match well the predicted values in table 3. The prescribed heat fluxes are therefore considered accurate.

The impingement point of the LSC can also be identified from the local peak in temperature seen on the upper boundary in figure 3. This is a result of the hot plumes released from the heated lower wall travelling with the mean wind. Further, we note that the direction of the LSC *at* the shear-free boundary following impingement is also visible from the superimposed velocity vectors in figure 3b.

We next examine the diagonal plane occupied by the large-scale circulation at $Ra = 5 \times 10^7$ shown in figure 4a. Similar to turbulent RBC in a cube, the large-scale circulation occupies the entire height of the domain. Further, the LSC creates recirculation zones in

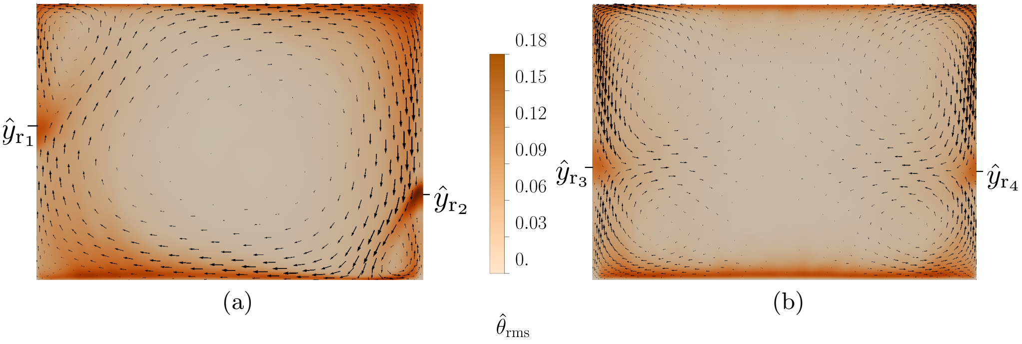

(a) (b)

FIGURE 4. Diagonal planes showing $\hat{\theta}_{\mathrm{rms}}$ fields at $Ra = 5 \times 10^7$: (a) plane containing the LSC and (b) the plane orthogonal to that shown in (a). The mean velocity vector field is superimposed for clarity.

opposite top and bottom corners. However, contrary to turbulent RBC in a cube, these recirculation zones are asymmetric in the current configuration. We define the coordinate of the lowest point of the upper recirculation zone as $\hat{y}_{r_1}$. Equivalently, the highest point of the lower recirculation zone is defined as $\hat{y}_{r_2}$. These values represent the $\hat{y}$ at which the vertical component of the mean velocity changes sign nearest the side-wall in figure 4a. From the same figure, the recirculation zone at the lower wall visibly occupies a smaller zone than its equivalent in the opposite corner, that is $\hat{y}_{r_2} < 1 - \hat{y}_{r_1}$. The explanation is in the role played by the shear-free boundary, accelerating the large-scale flow in the negative y-direction. The limits of the recirculation zones, $\hat{y}_{r_1}$ and $\hat{y}_{r_2}$, are provided in table 7 for the five cases. We observe that as Ra is increased, the recirculation zones become taller and thinner, as they are pushed towards the corner regions by the increasing strength of the LSC.

Figure 4b shows the orthogonal plane to that given in 4a. We observe four counter-rotating vortical cells, similar again to previous observations in wall-bounded turbulent RBC. However, contrary to turbulent RBC in a box (Foroozani *et al.* 2014), the counter-rotating vortical cells occupy more space in the upper volume of the pool than in the lower. Their size can be qualitatively inferred by the locations of the peak $\hat{\theta}_{\mathrm{rms}}$ on the side-walls. The vertical coordinate at which the upper and lower counter-rotating vortical cells interact is again found from the first $\hat{y}$ at which the vertical component of the mean velocity changes sign nearest the side-wall in figure 4b. For turbulent RBC in a box, this occurs at $\hat{y} = 0.5$, whereas for the current configuration this location is found closer to the lower wall; see $\hat{y}_{r_3} = \hat{y}_{r_4}$ in table 7. The explanation is the same as for the LSC plane; the rotating vortical cells accelerate towards the boundaries after impingement at the shear-free surface. This is visible from the vector field in figure 4b, showing stronger downward motion than upward. The structure of the LSC is thus visibly impacted by the presence of the free surface. We again provide values for the recirculation zone limits, $\hat{y}_{r_3}$ and $\hat{y}_{r_4}$, in table 7 and note that the counter-rotating vortical cells near the shear-free surface occupy an increasingly larger zone as Ra is augmented. To better visualize the LSC and the location of the points $\hat{y}_{r_i}$, $i = 1 - 5$, we plot in figure 5 time-averaged streamlines coloured by the vertical velocity, $\hat{v}$, for the $Ra = 5 \times 10^7$ case.

One consequence of the asymmetry is that the upper recirculation zone extends towards the mid-plane of the domain at $\hat{y} = 0.5$. To better understand the LSC, we therefore plot, in figure 6, the mean vertical velocity, $\langle \hat{v} \rangle$, across the diagonal containing the LSC at $\hat{y} = 0.4$. Therein, we observe the near-zero (vertical) velocity region in the centre of

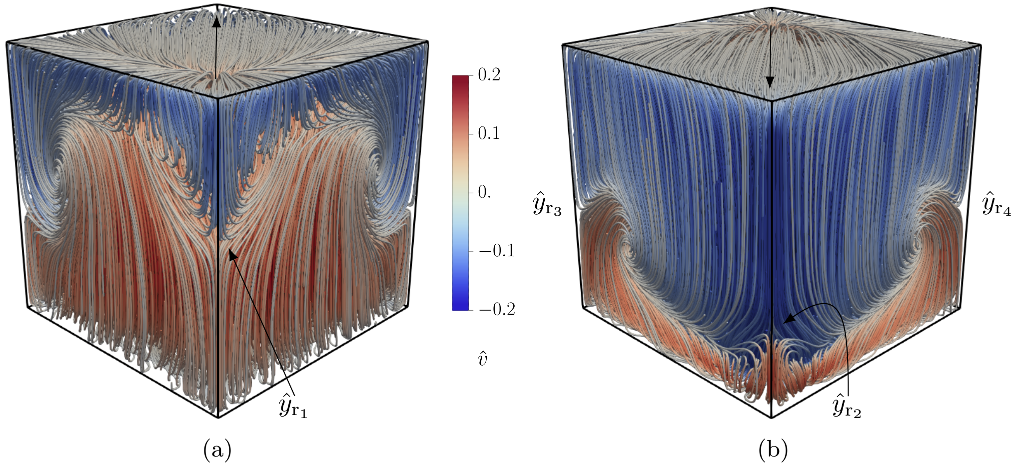

FIGURE 5. Time-averaged streamlines coloured by the vertical velocity, $\hat{v}$, for the $Ra = 5 \times 10^7$ case. We annotate the figure with the direction of the LSC on the free-slip upper boundary as well as the vertical limits of the recirculation zones.

Ra	$\hat{y}_{\mathrm{r}_1}$	$\hat{y}_{\mathrm{r}_2}$	$\hat{y}_{\mathrm{r}_3} = \hat{y}_{\mathrm{r}_4}$
7.5×10^6	0.55	0.26	0.42
1.5×10^7	0.52	0.27	0.42
5×10^7	0.51	0.35	0.41
9×10^7	0.50	0.38	0.40
1.3×10^8	0.53	0.37	0.40

TABLE 7. Vertical limits of the recirculation zones. The coordinates $\hat{y}_{\mathrm{r}_1}$ to $\hat{y}_{\mathrm{r}_4}$ are shown in figures 4 and 5.

the LSC, also visible in figure 4a. The peaks near the sidewalls correspond respectively to the upward, $\frac{x}{\sqrt{2}H} \approx 0.03$, and downward, $\frac{x}{\sqrt{2}H} \approx 0.97$, motions of the LSC. Instead of the symmetric peaks observed in the equivalent plot of Foroozani *et al.* (2017) (at $\hat{y} = 0.5$), here the shear-free boundary accelerates the fluid following impingement. This results in the magnitude of the downward velocity exceeding that of the upward. This can also be clearly observed in the vector field superimposed onto figure 4a. The insets in figure 6 show how the LSC is pushed towards the corner walls as Ra is increased; a trend also noted in both Cioni *et al.* (1997) and Foroozani *et al.* (2017) for confined turbulent RBC.

It is worth adding that LSC reorientations are a known phenomenon in thermal convection configurations such as turbulent RBC (Cioni *et al.* 1997; Brown & Ahlers 2006; Foroozani *et al.* 2017). We also observed such events in our simulations. However, since this paper does not concentrate on LSC reorientations, all results presented herein are from simulations whose time-averaging periods correspond to a stable LSC. It is worth adding that our simulations suggest fewer reorientation events occur in the current set-up compared to that of turbulent RBC. It is thus tempting to imply that the free-slip upper boundary may reduce the number of LSC reorientations. In other words, playing a similar role to tilting the container, the free surface may encourage the LSC into a preferred orientation (Cioni *et al.* 1997; Brown & Ahlers 2006). However, more simulations are required over significantly longer time periods before conclusions should be drawn.

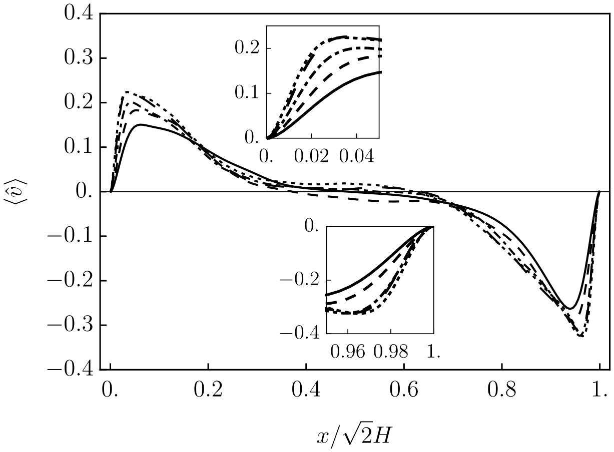

FIGURE 6. Plot of the mean dimensionless vertical velocity, $\langle\hat{v}\rangle$, along the diagonal line containing the LSC at $\hat{y} = 0.4$. The insets show zooms near the corner regions. The legend is as follows: $Ra = 7.5\times10^6$ (——), $Ra = 1.5\times10^7$ (- - -), $Ra = 5\times10^7$ (–·–·), $Ra = 9\times10^7$ (— —), and $Ra = 1.3\times10^8$ (·······).

We next present analysis of the rms of the vertical velocity fluctuations in the centre of the domain, $(v_{\text{rms}})_{\text{ctr}} = \sqrt{\langle v'v'\rangle_{\text{ctr}}}$. Non-dimensionalizing by ν_{ref}/H, provides the following local Reynolds number,

$$Re_{\text{ctr}} = \frac{(v_{\text{rms}})_{\text{ctr}}\, H}{\nu_{\text{ref}}}, \tag{6.1}$$

Values of Re_{ctr} are provided in table 6 and are plotted in figure 7a, where the associated power-law fit,

$$Re_{\text{ctr}} = 1.0\times10^{-3} Ra^{0.68}, \tag{6.2}$$

merits further discussion.

The turbulent RBC experiments of Daya & Ecke (2001) measured Re_{ctr} over 1.3 decades of Ra for cubic geometries and provided the power-law fit, $Re_{\text{ctr}} = Ra^{\beta}$, with $\beta = 0.36 \pm 0.05$. Whereas Foroozani *et al.* (2014) found numerically $Re_{\text{ctr}} = 0.31Ra^{0.39}$ over an increased range of Ra. Importantly, in both these studies the mean temperature in the domain remained constant as Ra was increased. As a result, the viscosity used for the non-dimensionalization in (6.1) was also constant between experiments (or simulations).

In contrast, the Rayleigh numbers investigated in this paper are updated via changes in thermal boundary conditions. As such, both T_{ref} and ν_{ref} vary significantly between cases, as shown in tables 3 and 4. We know this to be the cause of the discrepancy in the exponents because, according to our simulations, a power-law fit of the $(v_{\text{rms}})_{\text{ctr}}$ data reads,

$$(v_{\text{rms}})_{\text{ctr}} \propto Ra^{0.41}, \tag{6.3}$$

see also figure 7a. The exponent in (6.3) is in good agreement with Daya & Ecke (2001) and Foroozani *et al.* (2014) for turbulent RBC.

We also provide in table 6 the rms of the vertical velocity based on the combined volume-time averages; $(v_{\text{rms}})_{\text{xyz}} = \sqrt{\langle v'v'\rangle_{\text{xyz}}}$, as well as the associated global Reynolds number, Re. We see the same trend in the power-law fits for the global data where we have

$$Re = 1.0\times10^{-3} Ra^{0.73} \quad \text{and} \quad (v_{\text{rms}})_{\text{xyz}} \propto Ra^{0.49}. \tag{6.4}$$

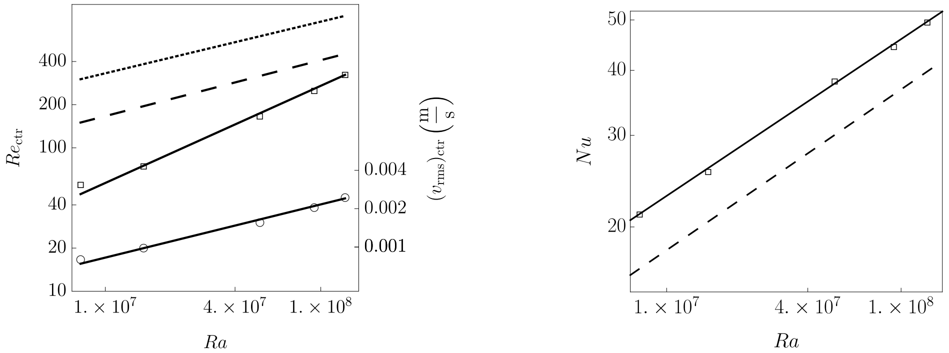

(a) Ra scaling of Re_{ctr} and $(v_{\mathrm{rms}})_{\mathrm{ctr}}$. The legend is as follows: Re_{ctr} data (□), $(v_{\mathrm{rms}})_{\mathrm{ctr}}$ data (○), the power-law fits to the present data: $Re_{\mathrm{ctr}} = 1.0 \times 10^{-3} Ra^{0.68}$ (——) above and $(v_{\mathrm{rms}})_{\mathrm{ctr}} \propto Ra^{0.41}$ (——) below, the power-law fit of Daya & Ecke (2001): $Re_{\mathrm{ctr}} = Ra^{0.36}$ (⋯⋯), the power-law fit of Foroozani *et al.* (2014): $Re_{\mathrm{ctr}} = 0.31 Ra^{0.39}$ (— —).

(b) Ra scaling of Nu. The legend is as follows: Nu data (□), power-law fit to the present data: $Nu = 0.178 Ra^{0.301}$ (——) and the power-law fit of Niemala *et al.* (2000): $Nu = 0.124 Ra^{0.309}$ (— —).

FIGURE 7. Ra-scaling plots

Our fit of $(v_{\mathrm{rms}})_{\mathrm{xyz}}$ matches well that of Scheel & Schumacher (2014) for turbulent RBC in cylindrical domains, according to which Re scales as Ra^{β}, with $\beta = 0.49 \pm 0.01$. Please note that, since $(v_{\mathrm{rms}})_{\mathrm{ctr}}$ and $(v_{\mathrm{rms}})_{\mathrm{xyz}}$ are dimensional quantities, only the exponents of the corresponding power laws are of interest here.

Similarly to Daya & Ecke (2001), the explored parameter space is limited to a rather short range of 1.25 Ra decades, what is of interest however is the similar scaling for the v_{rms} observed both globally and in the centre of the domain. Of course, the current set-up differs from turbulent RBC due to the free-slip upper boundary. The similar scaling for the rms of vertical velocity fluctuations in the bulk suggests that, away from the boundaries, the behavior of this fluctuating quantity is similar for the two configurations.

The dimensionless heat transfer across any $x - z$ plane is measured by the local Nusselt number, Nu_y, and is calculated from the sum of two contributions as follows,

$$Nu_y \;=\; \underbrace{\sqrt{RaPr}\,\langle \hat{\rho}\hat{v}\hat{\theta}\rangle_{xz}}_{Nu_{\mathrm{conv}}} \; \underbrace{-\langle \hat{\lambda}\frac{\partial \hat{\theta}}{\partial \hat{y}}\rangle_{xz}}_{Nu_{\mathrm{diff}}} \;. \tag{6.5}$$

This relation is found from time and area-averaging of the dimensionless form of the energy equation (2.3). The volume-averaged (global) Nusselt, Nu, is found from

$$Nu \;=\; \sqrt{RaPr}\,\langle \hat{\rho}\hat{v}\hat{\theta}\rangle_{xyz} \; - \langle \hat{\lambda}\frac{\partial \hat{\theta}}{\partial \hat{y}}\rangle_{xyz}. \tag{6.6}$$

For the flow in question, a statistically stationary solution gives Nu_y as constant and further equal to Nu. Indeed, for all examined cases, our simulations predicted constant Nu_y and in excellent agreement with Nu, the values of which are provided in table 6. Moreover, for all cases investigated, the global value after 150 free-fall times, or half the averaging time, changed by less than 1%. This finding suggests that the time-averaging interval is indeed sufficient.

The contributions of the convective and diffusive components of Nu_{y} are shown in

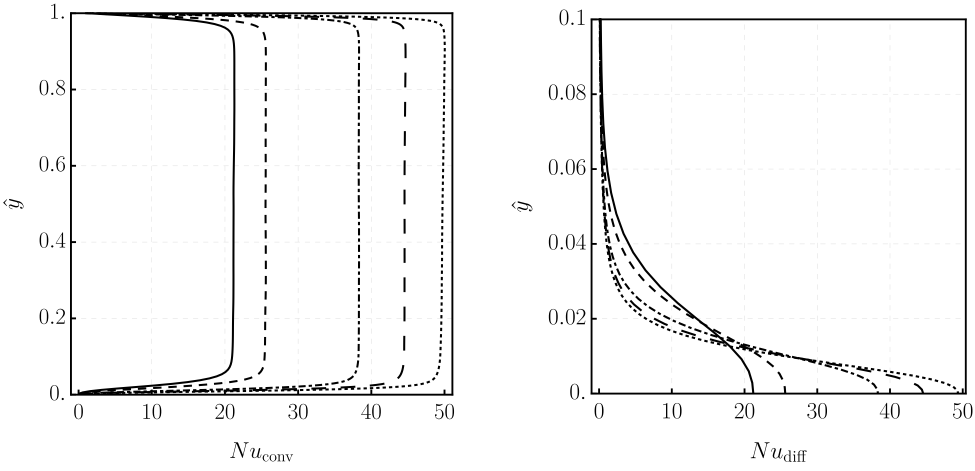

(a) (b)

FIGURE 8. Plots of the time and area-averaged components of Nu_y. (a) Nu_{conv} across the vertical direction and (b) Nu_{diff} zoom on lower boundary. The legend is as follows: $Ra = 7.5 \times 10^6$ (——), $Ra = 1.5 \times 10^7$ (- - -), $Ra = 5 \times 10^7$ (-·-·), $Ra = 9 \times 10^7$ (— —), and $Ra = 1.3 \times 10^8$ (······).

figures 8a and 8b respectively. The convective component, Nu_{conv}, tends to a non-zero, albeit negligibly small, value inside the thermal boundary layers and is the dominant contribution away from the walls. For the diffusive component, Nu_{diff}, only the near-wall contribution is shown, as it is negligible in the bulk. The definitions (6.5) and (6.6) take into account the variable density and thermal conductivity of the working fluid. However, these thermodynamic properties vary by a maximum of only 1.5% and 2% respectively and hence the non-Oberbeck-Boussinesq effect on Nu is very small for the flow considered.

With respect to the scaling with Ra we provide figure 7b where we find a power-law fit of

$$Nu = 0.178 Ra^{0.301}, \tag{6.7}$$

over 1.25 decades of Ra. Again, although the explored parameter space could be considered limited, what is of interest here is the excellent agreement with the exponent of Niemala *et al.* (2000) who obtained $Nu = 0.124 Ra^{0.309}$ for turbulent RBC. As Nu is a measure of the total (convective plus diffusive) heat transfer to diffusive heat transfer, the increased prefactor in our scaling is a result of the reduced number of hydrodynamic boundary layers present; see also the relevant discussion in Straus (1973).

6.2. *Flow statistics*

In this section we compare vertical profiles of time and area-averaged flow fields. For comparison against the more general thermal convection configuration of evaporative cooling, figure 1a, we use the experimental references of Katsaros *et al.* (1976) and Flack *et al.* (2001). Equivalently, for turbulent RBC, figure 1b, we use the DNS results of Kerr (1996). Finally, for comparisons against the set-up most similar to ours, we select Zikanov *et al.* (2002). In this latter paper, numerical experiments of turbulent convection driven by surface cooling were carried out in a domain with periodicity in the x and z directions.

The profiles of the rms of the velocity components are presented in figure 9. Concerning the rms of the vertical velocity fluctuations, $\hat{v}_{\mathrm{rms}}$, an almost parabolic profile is observed in figure 9a with zero values at the boundaries rising steeply towards a maximum in the

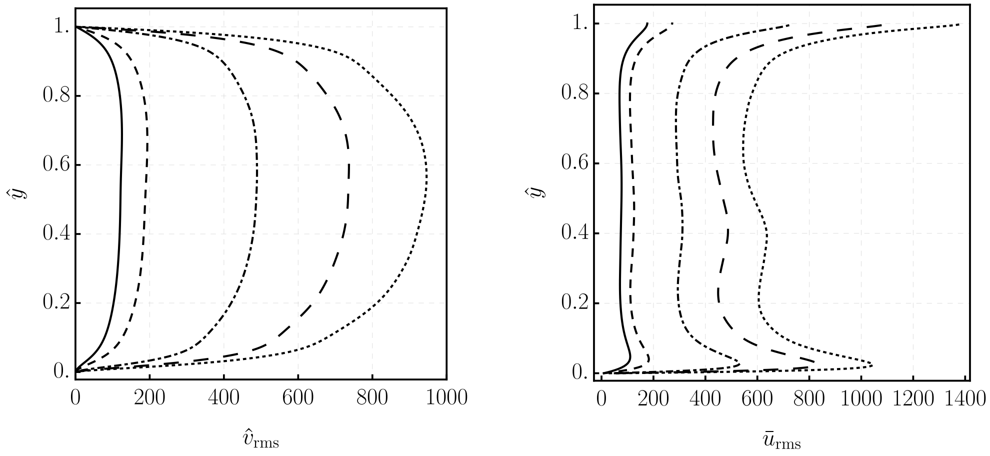

(a) (b)

FIGURE 9. Plots of the rms of velocity fluctuations across the vertical direction: (a) rms of vertical velocity fluctuations, $\hat{v}_{\mathrm{rms}}$, (b) rms of in-plane velocity fluctuations, $\bar{u}_{\mathrm{rms}}$. The velocities have been made dimensionless using ν_{ref}/H. The legend is as follows: The legend is as follows: $Ra = 7.5 \times 10^6$ (——), $Ra = 1.5 \times 10^7$ (- - -), $Ra = 5 \times 10^7$ (–·–·), $Ra = 9 \times 10^7$ (— —), and $Ra = 1.3 \times 10^8$ (······).

bulk. Overall, the profiles are similar to those for the flows seen in turbulent RBC of Kerr (1996) and also to those reported by Zikanov *et al.* (2002), which had a shear-free upper boundary.

However, contrary to the profile in Kerr (1996) and Zikanov *et al.* (2002) who both considered periodic domains, the profile is not fully symmetric with respect to the mid-plane $\hat{y} = 0.5$. This may be attributed to the non-periodic nature of our flow and the fact that averages are taken across a horizontal which includes side-wall boundary layers. On the other hand, we note that the free-slip condition has no significant effect on the profile of $\hat{v}_{\mathrm{rms}}$ close to the upper boundary. This is due to the fact that the vertical velocity component prescribed at both rigid walls and free-slip boundaries is zero.

In figure 9b we observe the profile of the fluctuating component of the in-plane velocity defined as follows,

$$\bar{u}_{\mathrm{rms}} = \sqrt{\langle \hat{u}'^2 + \hat{w}'^2 \rangle}_{xz} \, . \tag{6.8}$$

There is a clear asymmetry observed in the profile of the rms of in-plane velocity fluctuations, where a hydrodynamic boundary layer is visible near the lower wall only. The shear-free upper boundary results in the maximum in-plane velocity being found at the surface, in line with figure 3b showing the presence of strong surface currents. This observation has also been made experimentally by Flack *et al.* (2001) investigating turbulent structures in evaporative cooling. The near-flat bulk profile observed in the current configuration is different to the bulk profile seen by Kerr (1996) and later Zikanov *et al.* (2002), where both noted a characteristic dip in the bulk. This feature of our configuration is attributed to the container geometry, with its side-wall boundaries leading to the formation of the counter-rotating vortical cells seen in figure 4b. This flow structure results in higher rms values of in-plane velocity in the bulk. In fact, the maximum bulk value seen in figure 9b corresponds to the vertical position at which the counter-rotating vortical cells interact, $\hat{y}_{\mathrm{r}_3} = \hat{y}_{\mathrm{r}_4}$, provided in the last column of table 7.

The hydrodynamic boundary layer created by the shear of the large-scale circulation has a height, $\hat{\delta}_{\boldsymbol{u}}$. According to Kerr (1996) and Xin & Xia (1997) this height can be

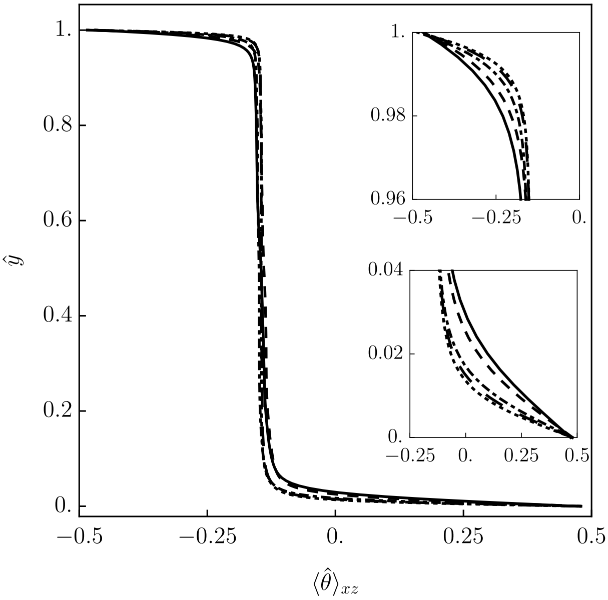

FIGURE 10. Plots of the mean normalized temperature, $\langle\hat{\theta}\rangle_{xz}$, across the vertical direction. The top and bottom insets are zooms on the upper and lower boundary layers respectively. The legend is as follows: $Ra = 7.5 \times 10^6$ (——), $Ra = 1.5 \times 10^7$ (- - -), $Ra = 5 \times 10^7$ (-·-·), $Ra = 9 \times 10^7$ (— —), and $Ra = 1.3 \times 10^8$ (······).

estimated from the local peak in $\bar{u}_{\rm rms}$ for which we provide values in table 6. It is confirmed that, at the lower boundary, the hydrodynamic layer is substantially thicker than the thermal one, as expected for $Pr > 1$. Further, as a result of the increasing shear generated by the LSC, $\hat{\delta}_{\boldsymbol{u}}$ is negatively correlated with Ra.

The profiles of the mean normalized temperatures are presented in figure 10, with the insets showing the boundary layers at the upper boundary and lower wall. We first observe that the normalized temperature in the bulk (or centre) of the flow, $\hat{\theta}_{\rm c}$, is smaller than the reference (or mean), $\hat{\theta}_{\rm m} = (\hat{\theta}_{\rm int} + \hat{\theta}_{\rm low})/2 = 0$. In other words, the mean temperature profile is shifted towards the temperature of the cold upper boundary. Conversely, Ahlers *et al.* (2006) showed that with water as the working fluid, the non-Oberbeck-Boussinesq effect in turbulent RBC results in $\hat{\theta}_{\rm c} > \hat{\theta}_{\rm m}$. That is, if variable thermodynamic properties are taken into account in turbulent RBC, the result is a mean bulk temperature shifted towards that at the hotter lower wall. These two statements taken together suggest that the free-slip and non-Oberbeck-Boussinesq effects are competing with the former being dominant. A similar observation was reported in Hay & Papalexandris (2019) for flows with a shear-free boundary under non-Oberbeck Boussinesq conditions but with a fixed upper boundary temperature. We can therefore confirm that a shear-free upper boundary plays an important role in the thermal mixing in the pool, irrespective of whether the upper boundary temperature is fixed or spatially-variable. Further, the temperature drop from the bulk to the interface, $\Delta T_{\rm u}$, is shown to be 45% smaller than the temperature drop between the lower wall and the bulk, $\Delta T_{\rm l}$. This observation merits future experimental validation.

The rms plots of the normalized temperature fluctuations, $\hat{\theta}_{\rm rms}$, are provided in figure 11. The observed profile shows a single peak at the lower wall, a minimum value in the bulk and a maximum at the upper boundary. This is in contrast to turbulent RBC with fixed temperature boundaries which have zero $\hat{\theta}_{\rm rms}$ values *at* the boundaries and maximums defining the thermal boundary layer heights at the top and bottom near-wall regions. In our configuration, at the lower wall, the thermal boundary layer is contained within its hydrodynamic equivalent. Within the thermal boundary layer, the rms of the temperature fluctuations increase with distance from the lower wall, as a result of the velocity fluctuations also increasing and more effectively stirring the fluid. The dip in the bulk is due to the ejected plumes losing their temperature contrast with the core fluid as they move through the domain (Tilgner *et al.* 1993). The maximum $\hat{\theta}_{\mathrm{rms}}$ at the shear free boundary can be explained by the peak in $\bar{u}_{\mathrm{rms}}$ at the same location; water is increasingly stirred up to the interface.

We denote by $\hat{\delta}_{\theta_{\mathrm{low}}}$ and $\hat{\delta}_{\theta_{\mathrm{int}}}$ the heights at the hot wall and cold interface respectively. The height of the thermal boundary layer on the lower wall can be defined as the location of the local peak in temperature variance (Kerr 1996). We then readily find $\hat{\delta}_{\theta_{\mathrm{low}}}$ from figure 11 and provide values in table 6. We observe however, that the maximum $\hat{\theta}_{\mathrm{rms}}$ across the vertical direction appears *at* the upper boundary; we must then estimate $\hat{\delta}_{\theta_{\mathrm{int}}}$ by another means. An alternative method is proposed by Katsaros *et al.* (1976), where the thermal boundary layer height at an evaporating interface is defined as follows,

$$\delta_{\theta_{\mathrm{int}}} = -\lambda_{\mathrm{w}} \frac{T_{\mathrm{int}} - T_{\mathrm{bulk}}}{\dot{q}''_{\mathrm{tot}}} , \tag{6.9}$$

with $\dot{q}''_{\mathrm{tot}}$ as the total heat flux, i.e. the sum of the convective and latent contributions, applied at the interface and λ_{w} as the thermal conductivity of water at the interface. Note that this quantity is calculated from equation (3.2) and the rounded values of $\overline{\partial T/\partial y|_{\mathrm{w}}}$ from table 2. The dimensional T_{bulk} is interpreted from figure 10 and we provide values for $\hat{\delta}_{\theta_{\mathrm{int}}}$ in table 6. A similar approach is used in the turbulent RBC literature for calculating a boundary layer thickness scale based on the local temperature gradients at the hot and cold walls (Ahlers *et al.* 2006; Stevens *et al.* 2010; Scheel & Schumacher 2014).

We next focus on the inhomogeneities between the upper and lower thermal boundary layers. In particular, $\hat{\delta}_{\theta_{\mathrm{low}}}$ is larger than $\hat{\delta}_{\theta_{\mathrm{int}}}$, in accordance with the observations made regarding the vertical mean temperature profile. This observation was also made in Hay & Papalexandris (2019) but for a fixed temperature upper boundary, as opposed to the spatially-variable interface temperature investigated here. We attribute the inhomogeneities to the presence of the shear-free boundary. Sun *et al.* (2008) state that the thermal boundary layers in turbulent RBC are not isolated from but modified (and stabilized) by the viscous shear of the LSC. This same shear also produces the hydrodynamic boundary layers which are dynamically coupled to their thermal equivalents. The asymmetry introduced by the differing hydrodynamic boundary conditions results in an asymmetric LSC whose modifying (and stabilizing) capacity on the thermal boundary layers is, of course, impacted. The thinner thermal boundary layer above is therefore a result of the increase in LSC velocity and associated shear. Further, and with similar reasoning, the thermal boundary layer thinning effect with increasing Ra is confirmed from table 6.

We also provide in table 6 the estimation for thermal boundary layer heights in RBC between two rigid plates, $\frac{1}{2Nu}$, which assumes symmetry between the upper and lower boundaries. We find that despite the asymmetry introduced by the shear-free surface, the relation $(\hat{\delta}_{\theta_{\mathrm{low}}} + \hat{\delta}_{\theta_{\mathrm{int}}}) \approx \frac{1}{Nu}$ still holds.

In terms of third-order statistics we provide in figure 12 the skewness of the normalized temperature,

$$\hat{S}_{\theta} = \frac{\langle \hat{\theta}'^{3} \rangle_{xz}}{\hat{\theta}^{3}_{\mathrm{rms}}} . \tag{6.10}$$

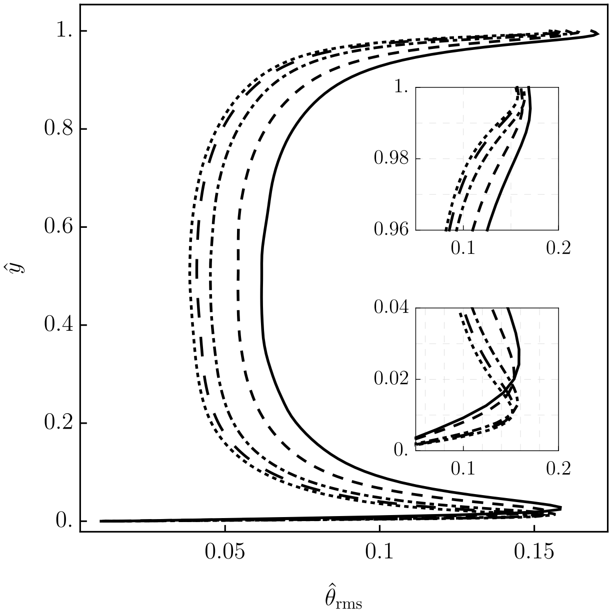

FIGURE 11. Plots of the rms of the normalized temperature fluctuations, $\hat{\theta}_{\mathrm{rms}}$, across the vertical direction. The top and bottom insets are zooms on the upper and lower boundaries respectively. The legend is as follows: $Ra = 7.5 \times 10^6$ (——), $Ra = 1.5 \times 10^7$ (- - -), $Ra = 5 \times 10^7$ (-·-·), $Ra = 9 \times 10^7$ (— —), and $Ra = 1.3 \times 10^8$ (······).

We observe a negative skewness profile near the lower wall inside the thermal boundary layer turning positive just outside, similar to that seen in turbulent RBC (Castaing *et al.* 1989). There is then a change in sign at $\hat{y} \approx 0.4$ and contrary to the situation at the lower wall, the upper boundary skewness is never positive. This is in contrast to turbulent RBC between rigid plates where the profile is symmetric and where the change in sign occurs at the mid-height, i.e. $\hat{y} = 0.5$ (Kerr 1996). The uniquely negative skewness underneath the evaporating surface is a feature of evaporative cooling and seen experimentally in Katsaros *et al.* (1976). Further, the predominantly negative skewness profile represents more intense and frequent plume formation at the shear-free surface which then travel in the negative direction, similar to the observation reported by Zikanov *et al.* (2002). In summary, the skewness profile in figure 12 shows unique traits of the current turbulent convection configuration, which borrows characteristics from both turbulent RBC and evaporative cooling.

7. Summary and conclusions

In this article direct numerical simulations have been carried out of a thermal convection set-up with similarities to both turbulent Rayleigh-Bénard convection and evaporative cooling. The flow is a simplified model of the water-side thermal mixing occurring beneath an air-water interface during high temperature evaporation of spent-fuel pools. Five cases have been evaluated with the heat fluxes applied at the upper boundary approximating the evaporative heat loss. For the geometry chosen, a sixteenfold increase in evaporation rate induces a 1.25 decade change in Rayleigh number for the convective flow beneath the interface. For each case investigated, the statistically steady time-averaged temperature at the upper boundary has significant spatial variation, but the time and area-averaged

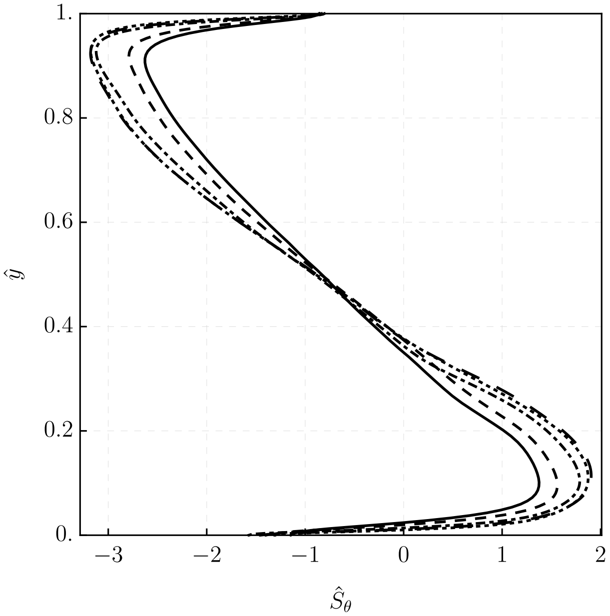

FIGURE 12. Plots of the normalized temperature skewness, $\hat{S}_\theta$, across the vertical direction. The legend is as follows: $Ra = 7.5 \times 10^6$ (——), $Ra = 1.5 \times 10^7$ (- - -), $Ra = 5 \times 10^7$ (-·-·), $Ra = 9 \times 10^7$ (— —), and $Ra = 1.3 \times 10^8$ (······).

value matches well with the predicted temperatures corresponding to the prescribed heat fluxes.

The upper boundary is also shear-free and as such, is an approximation of a free surface. One consequence of the free slip at the upper boundary is the asymmetric large-scale circulation. The large-scale circulation impinges the upper surface near one corner, where it is subsequently accelerated, suggesting the presence of strong surface currents, before falling back down in the opposite corner. This acceleration leads to inhomogeneous recirculation zones in the cubic geometry, which become taller and thinner with increasing Ra. As a result, the structure of the large-scale circulation is effected by the presence of the free surface.

Another impact of the shear-free surface is an increase in convective heat transfer, Nu. The provided power-law fit, $Nu = 0.178 Ra^{0.301}$, shows a similar exponent to turbulent RBC but with an increased prefactor due to the reduced number of hydrodynamic boundary layers. Our definition of Nu takes into account the variable density and thermal conductivity, however these thermodynamic properties vary by a maximum of only 1% and 2% respectively and hence the non-Oberbeck-Boussinesq effect on Nu is very small for the flow considered.

Further, a shear-free upper boundary is shown to introduce inhomogeneities in the heights of thermal boundary layers between the lower wall and upper boundary. This is in spite of taking into account the variable thermodynamic properties of water which tend to have the opposite effect. Such an observation is novel for the current set-up with a spatially-variable temperature boundary condition on the upper surface.

The modelled flow is an idealized system whereby the evaporation rate at the interface, although representative in an overall sense, is applied uniformly; the evaporation rate is constant in time and space. For a more realistic dynamic boundary condition based on local surface temperatures, a similar time and area-averaged interface temperature is expected to emerge and will be the focus of future research.

The authors gratefully acknowledge the financial support of Bel V, a subsidiary of the Belgian Federal Agency of Nuclear Control. The present research benefited from computational resources made available on the Tier-1 supercomputer of the Fédération Wallonie-Bruxelles, infrastructure funded by the Walloon Region under the grant agreement n° 1117545.

Declaration of Interests. The authors report no conflict of interest.

REFERENCES

Ahlers, G., Brown, E., Araujo, F.F, Funfschilling, D., Grossmann, S. & Lohse, D. 2006 Non-Oberbeck-Boussinesq effects in strongly turbulent Rayleigh-Bénard convection. *J. Fluid Mech.* **569**, 409–445.

Ahlers, G., Grossman, S. & Lohse, D. 2009 Heat transfer and large scale dynamics in turbulent Rayleigh-Bénard convection. *Rev. Mod. Phys.* **81** (2), 503–537.

Batchelor, G. K. 1959 Small-scale variation of convected quantities like temperature in turbulent fluid part 1. general discussion and the case of small conductivity. *J. Fluid Mech.* **5** (1), 113–133.

Boelter, L. M. K., Gordon, H. S. & Griffin, J. R. 1946 Free evaporation into air of water from a free horizontal quiet surface. *Ind. Eng. Chem.* **38** (6).

Bower, S. M. & Saylor, J. R. 2009 A study of the Sherwood-Rayleigh relation for water undergoing natural convection-driven evaporation. *Int. J. Heat Mass Tran.* **52**, 3055–3063.

Brown, E. & Ahlers, G. 2006 Rotations and cessations of the large-scale circulation in turbulent Rayleigh–Bénard convection. *J. Fluid Mech.* **568**, 351–386.

Bukhari, S. J. K. & Siddiqui, M. H. K. 2006 Turbulent structure beneath air-water interface during natural convection. *Phys. Fluids* **18** (3), 035106.

Castaing, B., Gunaratne, G., Heslot, F., Kadanoff, L., Libchaber, A., Thomae, S., Wu, X.-Z., Zaleski, S. & Zanetti, G. 1989 Scaling of hard thermal turbulence in Rayleigh-Bénard convection. *J. Fluid Mech.* **204**, 1–30.

Chavanne, X., Chillà, F., Castaing, B., Hébral, B., Chabaud, B. & Chaussy, J. 1997 Observation of the ultimate regime in Rayleigh-Bénard convection. *Phys. Rev. Lett.* **79**, 3648–3651.

Cioni, S., Ciliberto, S. & Sommeria, J. 1997 Strongly turbulent Rayleigh-Bnard convection in mercury: comparison with results at moderate Prandtl number. *J. Fluid Mech.* **335**, 111–140.

Daya, Z. A. & Ecke, R. E. 2001 Does turbulent convction feel the shape of the container? *Phys. Rev. Lett.* **87** (218), 184501.

Deardroff, J. W. & Willis, G. E. 1967 Investigation of turbulent thermal convection between horizontal plates. *J. Fluid Mech.* **28**, 675–704.

Flack, K. A., Saylor, J. R. & Smith, G. B. 2001 Near surface turbulence for evaporative convection. *Phys. Fluids* **13** (11), 3338–3345.

Foroozani, N., Niemala, J. J., Armenio, V. & Sreenivasan, K. R. 2014 Influence of container shape on scaling of turbulent fluctuations in convection. *Phys. Rev. E* **90**, 063003.

Foroozani, N., Niemela, J. J., Armenio, V. & Sreenivasan, K. R. 2017 Reorientations of the large-scale flow in turbulent convection in a cube. *Phys. Rev. E* **95**, 033107.

Georgiou, M. & Papalexandris, M. V. 2018 Direct numerical simulation of turbulent heat transfer in a T-junction. *J. Fluid Mech.* **845**, 581–614.

Grötzbach, G. 1983 Spatial resolution requirements for direct numerical simulation of the Rayleigh-Bénard convection. *J. Comput. Phys.* **49**, 241–264.

Hay, W. A. & Papalexandris, M. V. 2019 Numerical simulations of turbulent thermal convection with a free-slip upper boundary. *Proc. R. Soc. A* **475** (20190601).

Howard, L. N. 1966 Convection at high Rayleigh number. In *Applied Mechanics* (ed. Henry Görtler), pp. 1109–1115. Berlin, Heidelberg: Springer Berlin Heidelberg.

Issa, R. I. 1985 Solution of the implicitly discretized fluid flow equations by operator-splitting. *J. Comp. Phys.* **62**, 40–65.

Kaczorowski, M. & Wagner, C. 2008 Analysis of the thermal plumes in turbulent Rayleigh-Bénard convection based on well-resolved numerical simulations. *J. Fluid Mech.* **618**, 89–112.

Kaczorowski, M. & Xia, K. 2013 Turbulent flow in the bulk of Rayleigh-Bénard convection: small-scale properties in a cubic cell. *J. Fluid Mech.* **722**, 596–617.

Katsaros, K. B., Liu, W. T., Businger, J. A. & Tillman, J. E. 1976 Heat transport and thermal structure in the interfacial boundary layer measured in an open tank of water in turbulent free convection. *J. Fluid Mech.* **83**, 311–335.

Kerr, R. M. 1996 Rayleigh number scaling in numerical convection. *J. Fluid Mech.* **310**, 139–179.

Lemmon, E. W., Huber, M. L. & McLinden, M. O. 2010 *NIST Standard Reference Database 23: Reference Fluid Thermodynamic and Transport Properties - REFPROP*, 9th edn. National Institute of Standards and Technology, Standard Reference Data Program, Gaithersburg.

Lessani, B. & Papalexandris, M. V. 2006 Time accurate calculation of variable density flows with strong temperature gradients and combustion. *J. Comput. Phys.* **212**, 218–246.

Lessani, B. & Papalexandris, M. V. 2008 Numerical study of turbulent channel flow with strong temperature gradients. *Int. J. Numer. Method. H* **18**, 545–556.

Lienhard, IV, J. H. & Lienhard, V, J. H. 2019 *A Heat Transfer Textbook*, 5th edn. Mineola, NY: Dover Publications.

Lloyd, J. R. & Moran, W. R. 1974 Natural convection adjacent to horizontal surface of various planforms. *J. Heat Transfer* **96** (4), 443–447.

Lohse, D. & Xia, K. 2010 Small-scale properties of turbulent Rayleigh-Bénard convection. *Annu. Rev. Fluid Mech.* **42**, 335–364.

Majda, A. & Sethian, J. 1985 The derivation and numerical solution of the equations for zero-Mach number combustion. *Combust. Sci. Technol.* **42**, 185–205.

Marrero, T. R. & Mason, E. A. 1972 Gaseous diffusion coefficients. *Journal of Physical and Chemical Reference Data* **1** (1), 3–118.

Martin, J. & Migot, B. 2019 Experimental study of the surface evaporation rate of a heated water pool at high temperature using infrared thermography. In *18th International Topical Meeting on Nuclear Reactor Thermal Hydraulics*, pp. 2302–2313. Portland, Oregon: American Nuclear Society.

Mason, E. A. & Saxena, S. C. 1958 Approximate formula for the thermal conductivity of gas mixtures. *Phys. Fluids* **1** (5), 361–369.

Niemala, J. J., Skrbek, L., Sreenivasan, K. R. & Donnelly, R. J. 2000 Turbulent convection at very high Rayleigh numbers. *Nature* **404**, 837–840.

Oliviera, P. J. & Issa, R. I. 2001 An improved PISO algorithm for the computation of buoyancy driven flows. *Numer. Heat Tr. B-Fund* **40**, 473–493.

Papalexandris, M. V. 2019 On the applicability of Stokes' hypothesis to low-Mach-number flows. *Continuum Mech. Therm.* doi: 10.1007/s00161–019-00785-z.

Poling, B. E., Prausnitz, J. M. & O'Connell, J. P. 2001 *The properties of gases and liquids*. McGraw Hill.

Rhie, C. M. & Chow, W. L. 1983 Numerical study of the turbulent flow past an airfoil with trailing edge separation. *AIAA* **21** (11), 1525–1532.

Scheel, J. D. & Schumacher, J. 2014 Local boundary layer scales in turbulent Rayleigh-Bénard convection. *J. Fluid Mech.* **758**, 344–373.

Shishkina, O., Stevens, R., Grossman, S. & Lohse, D. 2010 Boundary layer structure in turbulent thermal convection and its consequences for the required numerical resolution. *New J. Phys.* **12** (7), 075022.

Siggia, E. D. 1994 High Rayleigh number convection. *Annu. Rev. Fluid Mech.* **26**, 137–168.

Spangenberg, W. G. & Rowland, W. R. 1961 Convective circulation in water induced by evaporative cooling. *Phys. Fluids* **4** (6), 743–750.

Stevens, R., Verzicco, R. & Lohse, D. 2010 Radial boundary layer structure and Nusselt number in Rayleigh-Bénard convection. *J. Fluid Mech.* **643**, 495–507.

STRAUS, J. M. 1973 On the upper bounding approach to thermal convection at moderate Rayleigh numbers. *Geophysical Fluid Dynamics* **5** (1), 261–281.

SUN, C., CHEUNG, Y.-H & XIA, K.-Q 2008 Experimental studies of the viscous boundary layer properties in turbulent Rayleigh-Bénard convection. *J. Fluid Mech.* **605**, 79–113.

TENNEKES, H. & LUMLEY, J.L. 1972 *A first course in turbulence*. Cambridge, MA: MIT Press.

TILGNER, A., BELMONTE, A. & LIBCHABER, A. 1993 Temperature and velocity profiles of turbulent convection in water. *Phys. Rev. E* **47**, R2253–R2256.

VERZICCO, R. & CAMUSSI, R. 2003 Numerical experiments on strongly turbulent thermal convection in a slender cylindrical cell. *J. Fluid Mech.* **477**, 19–49.

VOLINO, R. J. & SMITH, G. B. 1999 Use of simulataneous IR temperature measurements and DPIV to investigate thermal plumes in a thick layer cooled from above. *Exp. Fluids* **27**, 70–78.

WELLER, H. G., TABOR, G., JASAK, H. & FUREBY, C. 1998 A tensorial approach to computational continuum mechanics using object-oriented techniques. *Comput. Phys.* **12** (6), 620–631.

WILKE, C. R. 1950 A viscosity equation for gas mixtures. *J. Chem. Phys.* **18** (4), 517–519.

XIN, Y.-B. & XIA, K.-Q. 1997 Boundary layer length scales in convective turbulence. *Phys. Rev. E* **56**, 3010–3015.

ZIKANOV, O, SLINN, D. N. & DHANAK, M. R. 2002 Turbulent convection driven by surface cooling in shallow water. *J. Fluid Mech.* **464**, 81111.

Appendix A

In this appendix we first provide an example of the polynomial coefficients for calculation of the thermodynamic properties of water using (2.4). We then provide the gaseous mixture properties at a distance far from the interface and at the interface itself.

	c_4	c_3	c_2	c_1	c_0
$\frac{\rho}{p_0}$	-5.18×10^{-13}	7.79×10^{-10}	-4.63×10^{-07}	1.21×10^{-04}	-1.53×10^{-03}
μ	6.85×10^{-12}	-1.01×10^{-08}	5.59×10^{-06}	-1.39×10^{-03}	1.32×10^{-01}
λ	-7.96×10^{-11}	1.24×10^{-07}	-7.88×10^{-05}	2.40×10^{-02}	-2.20

TABLE A1. Polynomial coefficients for water thermodynamic properties at $Ra = 5 \times 10^7$. The values provided are a fit over the case specific temperature range of interest given in table 3. We note that the case-specific c_p is set constant at 4179, 4181, 4190, 4198, and 4202 J/kgK for cases $1 - 5$ respectively.

T_∞ (K)	p_0 (Pa)	RH (%)	$p_{\mathrm{v},\infty}$ (Pa)	ρ_∞ $\left(\frac{\mathrm{kg}}{\mathrm{m}^3}\right)$
298.15	101325	40	1270	1.18

TABLE A2. Gaseous mixture properties far from the interface. In this table, RH is the relative humidity (%), $p_{\mathrm{v},\infty}$ is the water vapour pressure after taking into account RH, and ρ_∞ is the mass-averaged gaseous mixture density far from the interface.

Case	T_{int} (K)	$p_{v,\mathrm{int}}$ (Pa)	$\rho_{\mathrm{int}}\left(\frac{\mathrm{kg}}{\mathrm{m}^3}\right)$
1	313.15	7400	1.14
2	318.15	9600	1.12
3	338.15	25100	1.06
4	348.15	38600	1.01
5	353.15	47400	0.99

TABLE A3. Gaseous mixture properties at the interface. In this table, $p_{v,\mathrm{int}}$ is the saturation vapour pressure at the mean interface temperature, T_{int}, and ρ_{int} is the interface mass-averaged gaseous mixture density.